

## Ground-layer snow clouds

G. Vali,\* D. Leon and J. R. Snider

*University of Wyoming, Laramie, Wyoming, USA*

\*Correspondence to: G. Vali, Department of Atmospheric Science, University of Wyoming, 1000 E. University Ave., Laramie, WY 82070, USA. E-mail: vali@uwyo.edu

Snow clouds forming directly over the ground and reaching depths of up to a kilometre have been observed with a W-band airborne radar. The phenomenon is referred to here as 'ground-layer snow cloud' (GSC). Most of the cases were observed over mountainous terrain but some were seen over nearly flat terrain. These snow clouds occurred over snow-covered ground. The temperature at their point of first appearance on rising slopes was in the range 0 to  $-10^{\circ}\text{C}$  with humidity close to water saturation. GSCs form within windy and highly turbulent surface layers, with specific features linked to sudden rises or dips in terrain. The most plausible explanation for the formation of the GSC is that snow particles lofted from the surface grow in the ice-supersaturated environment and mix throughout the turbulent layer. Sufficiently high humidity for crystal growth distinguishes these clouds from blowing snow in dry air. On the downwind sides of mountains, the snow clouds precipitate and evaporate. As for blowing snow, visibility within GSCs is greatly reduced. The GSC represents a form of horizontal water mass transport. When a GSC forms with other clouds present above it, as is frequently the case, there is a clear potential for those clouds to be seeded from below, thereby altering their evolution, precipitation distribution, and other impacts. Copyright © 2012 Royal Meteorological Society

*Key Words:* cloud ice; ice initiation; blowing snow

*Received 17 July 2011; Revised 14 December 2011; Accepted 16 December 2011; Published online in Wiley Online Library*

*Citation:* Vali G, Leon D, Snider JR. 2012. Ground-layer snow clouds. *Q. J. R. Meteorol. Soc.* DOI:10.1002/qj.1882

### 1. Introduction

This paper deals with an atmospheric phenomenon that is well known from everyday experience but has not been studied systematically, in large part because of the lack of suitable observational tools. Clouds of ice particles enveloping mountains, and at times over terrain of lesser relief, are frequent occurrences and are often believed to be falling snow. Data will be shown in this paper that make it clear that many of these situations involve a distinct layer of snow cloud of no more than a kilometre in depth and whose origin is not from higher clouds.

Radar observations of clouds and of precipitation have been key to our understanding of their composition and structures, and also to unravelling their formation and development. As a combined result of the nature of most

clouds and of the capabilities of radar systems, essentially all of these observations extend upward from a minimum of a few hundred metres above the ground. Characterization of fog and precipitation near the ground is usually based on *in situ* instruments. Relatively recent is the use of airborne W-band radar for the study of clouds and precipitation directly above (within tens of metres) the Earth's surface. Examples are the observations of drizzle from shallow clouds over land (Vali *et al.*, 1995) and, more extensively, over oceans (Stevens *et al.*, 2003; Wood *et al.*, 2011).

The observations reported here\* were made with a downward-pointing W-band radar carried on a research aircraft. Most, but not all, of the cases to be described

\*A preliminary report on these findings was given by Vali *et al.* (2008).

occurred over mountains and with some other clouds also present above the near-surface cloud layer. It is fairly certain that these near-surface clouds are composed mostly of ice crystals, but since no *in situ* observations are available from within the clouds the precise composition of the layers is unknown. In all cases that have been examined, the layer is characterized by a high degree of turbulence, in frequent contrast to the cloud layers above it. As will be seen from descriptions and analyses that follow, the essence of the phenomenon is well captured by referring to it as 'ground-layer snow cloud' (GSC).

Rogers and Vali (1987, RV87 in the following) reported on cap cloud cases when higher ice crystal concentrations were measured at the Elk Mountain Observatory than from aircraft about a kilometre above the mountain peak. That pattern is the reverse of what would be expected for ice crystals formed by nucleation, namely a monotonically increasing number concentration with decreasing temperature. Ice crystals were sampled with oil-coated slides and examined under a microscope. Crystals of tens to hundreds of micrometres in size were counted and only crystals with recognizable depositional growth habits (needles, columns, plates and dendrites) were accepted; irregular pieces of sintered and aged snow particles were also present but ignored. One possible explanation considered in RV87 was ice nucleation in the surface layer by aerosol that did not get transported higher up into the cloud top. Another mechanism examined in RV87 was rime formation on trees and associated ice particle production by splintering similar to the Hallett–Mossop process (Hallett and Mossop, 1974). As the most likely explanation for the high ice concentrations, RV87 posited that small pieces in the snow lofted from the surface upwind of the point of observation grew by deposition to regular crystal shapes while airborne.

On finding unexpectedly high concentrations of ice crystals in clouds and precipitation in the coastal region of Antarctica, Lachlan-Cope *et al.* (2001) considered the same potential explanations as RV87, plus seeding from higher clouds, and came to the same conclusion.

In retrospect, it is clear that the observations of RV87 and of Lachlan-Cope *et al.* (2001) were made in GSCs. As will be seen, the radar observations reported in this paper support the notion that lofted snow is responsible for the formation of these clouds with the important additional requirement that conditions be above saturation with respect to ice and perhaps a liquid cloud be present. Emphasis in this paper is on examining the details of the initiation of GSCs in order to gain some insight into factors governing their formation. The behaviour of the turbulent layer containing the GSC (Geerts *et al.*, 2011), the influence of the GSC on the cloud system in which it is embedded, and the transport of snow mass near the surface are also important topics but details of those issues are not addressed in this paper.

## 2. Data sources

Data were collected using the Wyoming Cloud Radar (WCR) installed on the Wyoming King Air aircraft, with fixed antennas pointing upward and downward so that vertical cross-sections of reflectivity and of Doppler velocity could be constructed in the plane of the aircraft path. Vertical velocities are reflectivity-weighted averages of air velocity plus particle fall velocity within the beam volume. Two

downward beams at different angles provided data for dual-Doppler analyses. The WCR operates at 3 mm wavelength and has a beam width of  $0.7^\circ$ . The best resolution along the beam is 15 m and profiles to 1.5, 3.0 or 4.5 km are collected at roughly every 3 m of flight distance. The closest range gate is at 75 m. The minimum detectable signal is roughly  $-25$  dBZ at 1 km range. Calibration of the radar was carried out using a corner reflector. Accuracy is estimated to be better than a factor of two over the range  $-25$  to  $+20$  dBZ, while short-term stability is about a factor of 1.3 (S. Haimov, private communication). Reflectivity data were thresholded at three to five times the noise level in an adaptive fashion that maximized data retention while assuring minimal noise contribution. Doppler velocity from pulse-pair phase shift was corrected for aircraft attitude variations and the horizontal wind component entering the beam was subtracted to derive the vertical component of particle velocities. Dual-Doppler analyses of winds were performed following the methods of Leon *et al.* (2006).

The King Air was equipped for measurement of state parameters (temperature, pressure, winds) and with probes for the measurement of cloud liquid water content (Gerber PVM and Rosemount icing probe), of cloud droplet size distributions and of ice particle shadow images (Particle Measuring System FSSP and 2D-C probes).

Flights were conducted over and in the vicinity of the Medicine Bow Mountains of southeast Wyoming, near  $41^\circ\text{N}$ ,  $106^\circ\text{W}$ . The mountain range is oriented roughly north–south with the highest peak at 3.6 km MSL, about 1.5 km above the valleys on either side. Data were also obtained over the Sierra Nevada range of Nevada near  $37^\circ\text{N}$ ,  $119^\circ\text{W}$  as part of the T-REX project (Grubišić *et al.*, 2008). Aircraft position is determined from GPS data. Geometric aircraft altitude is determined by integration of the hypsometric equation using measurements of temperature, specific humidity and pressure. Ground level derived from aircraft altitude and radar range to the ground generally agrees with topographic map values to within 10–30 m. In the radar cross-sections, a narrow horizontal band without echo (radar dead zone) indicates the flight path and a heavy dark line indicates the terrain.

Intermixed with the cross-range passes, soundings were made by the aircraft in the upwind and downwind valleys. These soundings were used to estimate the liquid condensation level (LCL) by assuming dry adiabatic lifting. The soundings were usually within about 1–2 h of the cross-range passes. That time delay, and variations across the study area (specially from the upwind to the downwind side of the mountain range), led to  $\pm 1^\circ\text{C}$  or more uncertainty in estimates of surface temperatures with a corresponding  $\pm 250$  m uncertainty in the lifted condensation level. The LCL was also estimated from flight-level measurements during overpasses of the GSC, by downward extrapolation of the saturated adiabatic lapse rate for the observed temperature and pressure. The LCL so determined agreed with the value derived from the soundings within about the error limits quoted above.

Supporting data were obtained from automated weather reports at airports near the flight areas, from the SNOTEL sites located in the Medicine Bow Mountains (<http://www.wcc.nrcs.usda.gov/nwcc/site?sitenum=367&state=wy>), from the Glacier Lakes Ecosystems Experiment Site (GLEES), near the top of the Medicine Bow Mountain (<http://www.fs.fed.us/rm/landscapes/Locations/Glees/>

Table 1. Summary of observations of GSCs.

Date	Time period (UTC)	Location	Number of flight legs	Base temperature $\pm 1$ ( $^{\circ}\text{C}$ )
18 Jan. 2006	2102–2250	MB	5	–6
26 Jan. 2006	2153–2207	MB	1	–8
27 Jan. 2006	2142–2252	MB and SM	6	–7
31 Jan. 2006	1335–1528	MB and SM	4	–3
2 Feb. 2006	1900–2200	MB	10	–5
5 Feb. 2006	1354–1543	MB	5	–10
9 Mar. 2006	1842–1852 and 2349–2353	SN	3	–9
10 Mar. 2006	0016–0030	SN	2	–9
14 Mar. 2006	1650–1750	SN	3	–8
15 Mar. 2006	0015–0145	SN	5	–4
26 Apr. 2006	1543–1820	WH and SN	5	–2
6 Feb. 2008	1753–1923	SH and MB	9	–6

MB, Medicine Bow Mountains, Wyoming; SM, Sierra Madre, Wyoming; SH, Shirley Mountains, Wyoming; SN, Sierra Nevada, California; WH, White Mountains, Nevada.

GLEES.shtml), and from the EPA/CASTNET (<http://java.epa.gov/castnet>) colocated with GLEES. Some data were also obtained from the University of Utah's MesoWest (<http://mesowest.utah.edu/cgi-bin/droman/mesomap.cgi?state=WY&rawsflag=3>).

The observations on which this paper is based were incidental to the main objectives of the flights and are, therefore, not optimized with respect to selection of flight altitude, length of pass and other considerations. Even so, flight plans were quite appropriate for these studies and the data are fully suitable for the analyses that follow.

### 3. Observations

From 11 flights, signatures of GSCs are evident in 48 radar cross-sections. Table 1 lists the dates, locations and times of these cases. Also listed in Table 1 as 'base temperature' are estimates of the temperature at the ground where the GSC is first detected (furthest upwind). The cases represent a variety of meteorological situations but all are from the winter months and are from high-altitude mountain regions. For about half of the cases to be discussed there were soundings of thermodynamic parameters upwind of the mountain range. For all of these cases, the potential temperature gradient in the 2 km thick layer between the upwind surface and mountain top height was positive ( $0\text{--}4\text{ K km}^{-1}$ ), indicating stable conditions but not excluding the possibility of convection arising above the condensation level. Evaluation of Sheppard's integral (Kleissl *et al.*, 2006) from these soundings showed that there was sufficient horizontal kinetic energy to transport surface air over the mountain. The examples presented here focus on the regions of formation of the GSCs with the aim of identifying the key processes involved.

The radar cross-sections to be presented can be considered 'snapshots' of the clouds, since the total sampling time for a cross-section is only 3–5 min – quite small compared to the times of travel of a parcel across the depicted fields. However, the observations do not represent steady-state situations. Cloud formations change quite rapidly in low-altitude winter clouds over mountains. The cross-sections presented in this paper are from flight legs along the wind direction prevailing at flight level, or the reverse, so the cross-sections approximately depict flow in the plane of observation, but some flow into and out of the plane of

observation cannot be ruled out. Wind direction is from left to right in the figures used in this paper.

#### 3.1. Medicine Bow Mountain deep cloud and GSC: 18 January 2006

The clouds forming over the Medicine Bow mountains on this day were fairly typical of wintertime, orographically induced deep clouds. Winds (from aircraft soundings over the upwind valley and from the NOAA profiler 50 km northwest of the flight zone) were generally from the west, from  $260^{\circ} \pm 10^{\circ}$  at both the 4.3 km and 5.2 km altitudes of aircraft passes across the mountain. Wind speeds increased from  $15\text{ m s}^{-1}$  at 3.5 km to  $30\text{ m s}^{-1}$  at 6 km over the upwind valley. Winds measured on a 15 m tower at GLEES, at 3.2 km altitude and about 10 km to the east of the ridgeline, fluctuated near  $10\text{ m s}^{-1}$ . All aircraft passes were either along or directly into the winds.

Temperature measured from the aircraft over the upwind valley was  $-5^{\circ}\text{C}$  at 3 km altitude, and in passes over the range it was  $-15^{\circ}\text{C}$  at 4.3 km and  $-20^{\circ}\text{C}$  at 5.2 km. Air temperature at GLEES was near  $-8.5^{\circ}\text{C}$  during the period. The mountain surface was covered by snow and possibly some snow also sat on the branches of the evergreen trees. There was no snowfall recorded by the USGS gauge at GLEES during the flight but an experimental hotplate device recorded about  $1\text{ mm h}^{-1}$  between 2020 and 2130 UTC. The CASTNET station data show  $-8.7^{\circ}\text{C}$  and relative humidity of 99%.

At the beginning of the flight, cloud tops reached to 7 km altitude, where a thin layer of cirrus was also detected. The west to east extent of the cloud was roughly 50 km. At the end of the flight, about 1 h 40 min later, cloud top height decreased to near 5 km and the horizontal extent decreased to about 30 km. The 90-percentile reflectivity values during five passes were 12, 7, 11, 6 and  $-6\text{ dBZ}$ . The sequence of radar cross-sections from the five passes is shown in Figure 1. The first pass was from west to east and each subsequent pass reversed direction. It can be seen in the radar data, and it is clearly seen in video and photo records taken from the cockpit, that a separate cloud layer was present by the time of the last two passes with tops at  $\sim 4.1\text{ km}$ , just below the 4.3 km altitude of the last pass. Figure 2 is one of these photos taken as the aircraft lined up at  $x = -34.5\text{ km}$  to make that last pass on the upwind side of the mountain. From this image, using the camera view angle ( $18^{\circ}$  in the vertical and

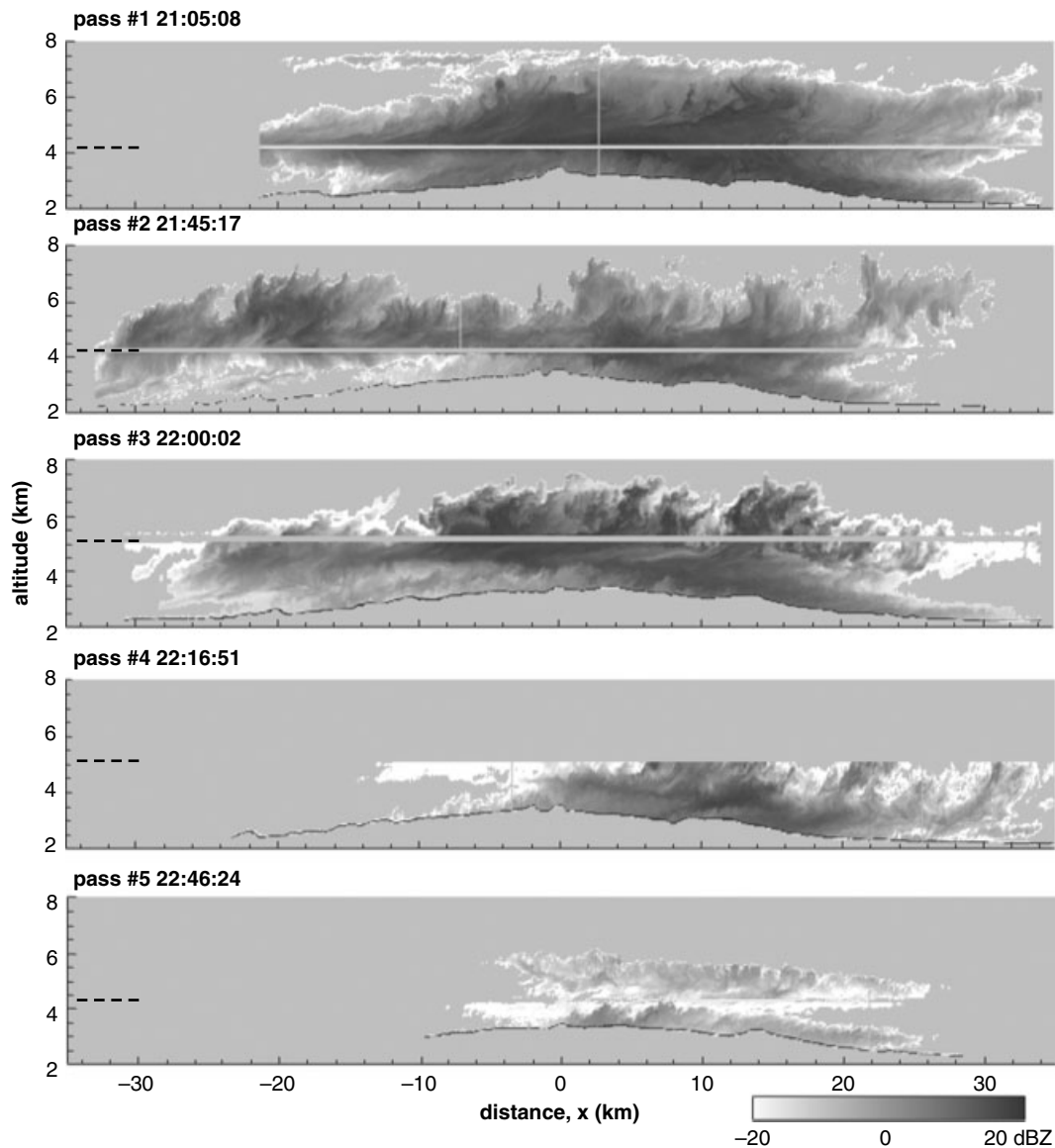


**Figure 1.** Vertical cross-sections of radar reflectivity from five aircraft passes on 18 January 2006 combining data from the upward and downward-pointing antennas. The thin bands at 4.3 km altitude (5.3 km in pass #5) indicate the aircraft flight level. For pass #4 only the antenna pointing downward was used, so that the image is truncated at the flight level. The images are shown with 4:1 vertical:horizontal scale compression. The distance scale is set to 0 km at the highest point of the terrain and the time given for each panel is the time of passage of this point. Times are in UTC. The grayscale for reflectivity applies to all panels. Wind is from left to right in this figure, as in all other cross-sections shown. Flight altitude is indicated in each frame by a short dashed line next to the ordinate.



**Figure 2.** Video frame from the aircraft cockpit at 4.3 km altitude and at  $x = -34.5$  km looking toward the east at the beginning of pass #5. The image shows that both the cloud layer above the aircraft and the more convective layer below extended much further west than where the radar echoes appear (near  $x = -8$  km).

$24^\circ$  in the horizontal) and estimated height of the clouds over the terrain, the leading edge of the altocumulus is estimated to be near  $-25$  km, about 15 km further than the westernmost edge of the radar echoes in pass #5.

Cloud liquid-water content (LWC) along the flight path was quite variable from pass to pass, as summarized in Table 2. Maximum LWC values were near  $0.3 \text{ g m}^{-3}$  and ice concentrations ranged up to  $20 \text{ L}^{-1}$ . While ice particles were ubiquitous, LWC was detected only over roughly a third of the flight legs. The maximum drop concentration measured was  $130 \text{ cm}^{-3}$ . The liquid condensation level, estimated from the aircraft sounding in the upwind valley taken between 2017 and 2054 UTC, was near 3.05 km altitude, below flight level. Calculations, using measured droplet concentrations and liquid water contents, show that these water clouds by themselves were undetectable by the radar.

A closer look at radar echoes near the mountain surface is shown in Figure 3. The most evident demonstration of

Table 2. Liquid water contents and ice particle concentrations along the flight path for 18 January 2006.

Pass #	LWC ( $\text{g m}^{-3}$ )	Location of LWC	Ice particle concentration ( $\text{L}^{-1}$ )	Flight altitude (km)
1	up to 0.3	Gradual increase toward 0 km and then decreasing	20 along most of pass	4.3
2	up to 0.3		5	4.3
3	0.05		20	5.2
4	0.25	Upslope portion	20	5.2
5	0.3	Only in turrets	1	4.3

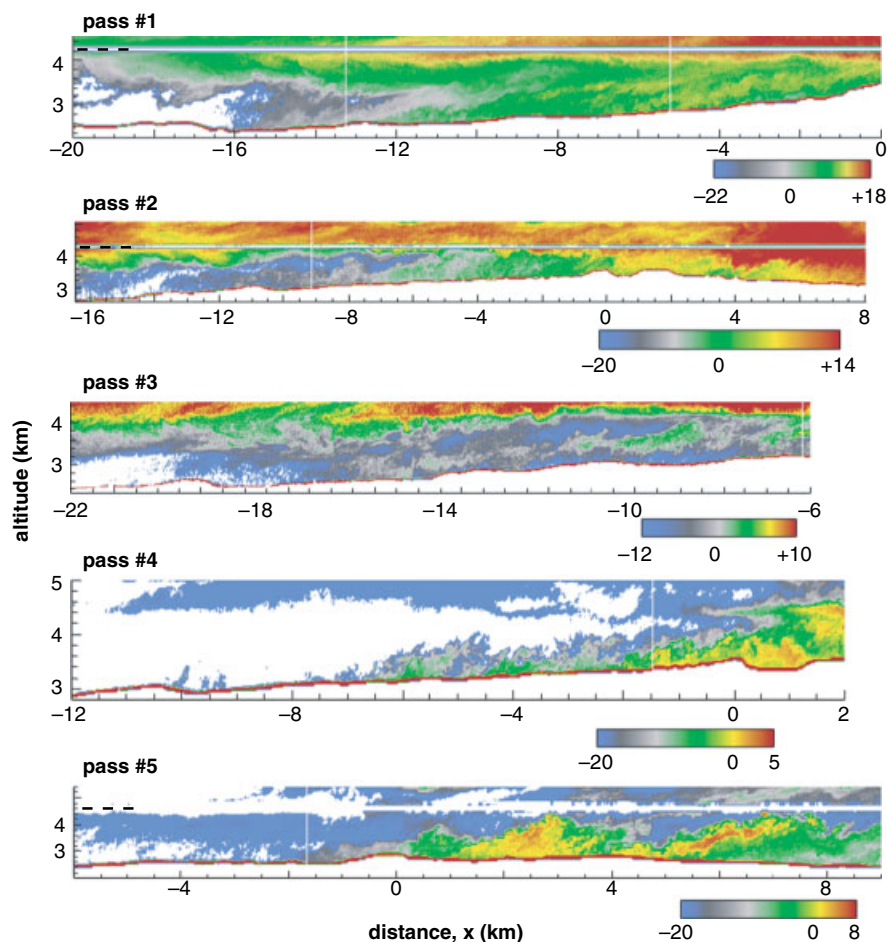


Figure 3. Enlarged segments from Figure 1 focusing on the regions with ground-layer snow clouds. These images are shown with a 1:1 vertical to horizontal scale. The reflectivity shading is variable from panel to panel in order to bring out the relevant echo features.

the GSC is seen in pass #4. Radar echoes right above the surface start at  $x = -10$  km with isolated puffs and form an unbroken field from  $x = -6$  km with embedded plumes. In the other passes, the GSC is seen to begin at different distances upwind from the ridge:  $x = -16$  km in pass #1,  $-12$  km in pass #2,  $-20$  km in pass #3, and only near  $x = -2$  km in pass #5. The average reflectivity within a layer 60–300 m above the surface is shown as a function of distance in Figure 4. The major increases in reflectivity with distance, from near  $-10$  to near  $+10$  dBZ, take place over similar distances in passes #1 to #4 and show a sharp jump in pass #5. In each case the depth of the GSC increases with distance, as seen in Figure 3.

Vertical Doppler velocities ( $w$ , positive upward) in the GSC are shown for passes #3 and #4 in Figure 5. Velocities range from  $-3$  to  $+2$   $\text{m s}^{-1}$  and both upward and downward velocities vary on many scales, with considerable variations on scales smaller than the reflectivity. This is consistent with the GSC forming in a turbulent boundary layer.

The transition from turbulence to more nearly quiescent conditions above is more abrupt than are reflectivity gradients there. No systematic changes with distance along the slope can be seen in the magnitudes and texture of velocities and no overall correlation could be found between reflectivity and velocity. By comparing Figure 3 with Figure 5, it is seen that there are numerous small regions (of order 100 m) with high reflectivity and upward velocity; for example, local echo maxima at  $x = -9$  km in pass #3 and at  $x = -10$  km in pass #4. But there are also similar high-reflectivity regions with downward velocities. Sudden rises in the terrain induce upward velocities: at  $x = -14$  km in pass #3, at  $x = 0$  and  $x = 1$  km in pass #4.

### 3.2. GSC over nearly flat terrain: 6 February 2008

This case is notable mostly because the observations were made at a location that has much less vertical relief than the preceding case. It is from an area about 40 km to the north

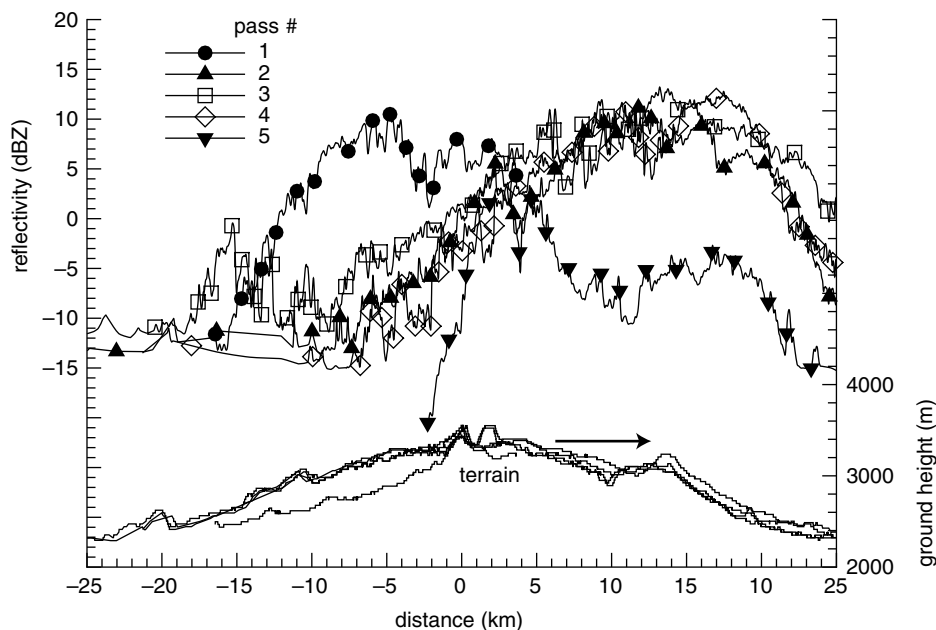


**Figure 4.** Average reflectivity 60–150 m above the surface (left-hand scale) as a function of distance for the radar data shown in Figure 1. Lines in the lower half of the graph (right-hand scale) show the terrain height derived from the radar echo during the different passes.

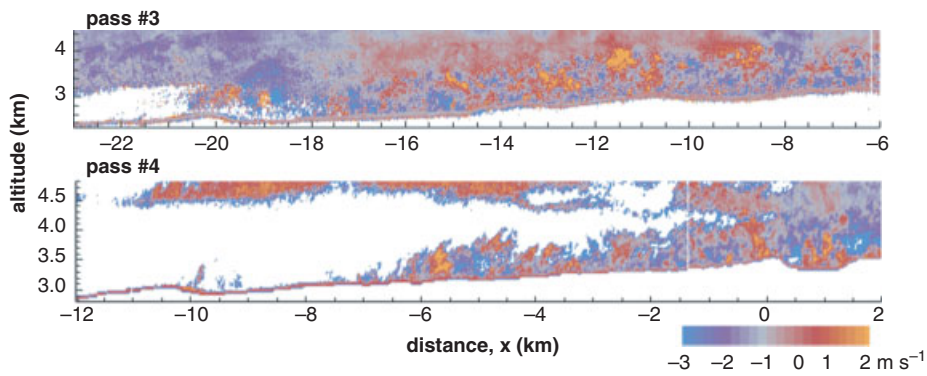
from the north end of the Medicine Bow range. Shirley Mountain ( $42^{\circ} 10'N$ ,  $106^{\circ} 35'W$ ) is somewhat of an isolated peak. It rises to 2.7 km, about 600 m above the surrounding terrain. The flight legs did not go over the highest part of the mountain, so the maximum terrain differences are only about 300 m. Three flight legs will be discussed here, each one along a slightly different ground track but within a few degrees of the  $290^{\circ}$  winds. Wind speed between the 3.6 and 4.1 km flight levels varied between 15 and  $25 \text{ m s}^{-1}$ . From temperatures observed at flight level and assuming a dry adiabatic lapse rate, the surface temperature is estimated to have been near  $-6^{\circ}\text{C}$ .

Figure 6 shows the reflectivity field for pass #1 (1726 UTC) over terrain decreasing in height. Highly structured echo fills a 500 m layer above the ground at the beginning. The layer deepens with distance, the highest reflectivity region rises to the top of the layer and the pattern becomes smoother. Past about  $x = 15 \text{ km}$  the echo weakens, indicating dissipation by precipitation and sublimation. A video frame looking toward the cloud from the downwind side (included in Figure 6, the view is toward the left of the figure), as the aircraft approached the echo region at 3.6 km altitude, shows a smoothly topped wave cloud which is dense in appearance and is likely to have contained liquid cloud droplets. The cloud did not reach the flight altitude. Data from later passes support the presence of an altostratus layer above flight level.

The main features of interest in the second pass (1738 UTC) were two small patches of locally high reflectivity which may have arisen as a result of the GSC penetrating into the cloud above it and which were traversed by the aircraft. Figure 7 shows the reflectivity and velocity fields for this pass. Within the thin cloud layer near 3.6 km altitude, the aircraft passed through a region of liquid water content of about  $0.1 \text{ g m}^{-3}$  between  $x = -3$  and  $x = 0 \text{ km}$ . Except in the two distinct patches of about 200 m horizontal extent, marked in Figure 7 with vertical arrows, no ice particles were detected in the region of water cloud. At those patches ice concentration along the flight line jumped to  $\sim 50 \text{ L}^{-1}$

with crystal sizes of 150–200  $\mu\text{m}$  and the reflectivity was 20 dB higher than outside those regions. Images from the 2D-C probe are shown above the arrows in Figure 7; the images suggest that the crystals were hexagonal plates. The patches did not extend downward past the radar dead-zone (75 m) along the aircraft flight level. Even so, the appearance of the patches just over the area where the GSC rose to the flight level and higher makes it likely that turrets rising from the GSC penetrated the overlying cloud just prior to the time of data collection. Temperature at flight level before cloud penetration was  $-13^{\circ}\text{C}$  and dropped to  $-18^{\circ}\text{C}$  within the cloud, indicating that the cloud was located below an inversion. A sharp increase in the level of turbulence accompanied the cloud penetration, supporting the likelihood that the patches of ice were transported from the GSC below. Further downwind along the flight track, between  $x = 2$  and  $x = 5 \text{ km}$ , ice concentration at flight level rose to a fairly uniform  $1.5 \text{ L}^{-1}$  with sizes also fairly uniform near 400  $\mu\text{m}$ . The velocity field (lower panel in Figure 7) is also interesting in that the depth of the turbulent layer decreased on the downward slope, past  $x = 0 \text{ km}$ , to only about 200 m over the flat terrain, at  $x > 4 \text{ km}$ . The high-reflectivity patches near  $x = -2 \text{ km}$  bear some similarity to the observations described in RV87 (Figure 7 of that paper).

The third pass extended further upwind so that the region of initial formation of the GSC was also observed, as can be seen in Figure 8. Also, this pass was over terrain of only minor relief. At this time, the altostratus at 3 km altitude is nearly continuous, but shows evidence of wave activity in its thinning and thickening. The GSC exhibits a similar character to other cases, including the presence of rising plumes, specially from about  $x = 3 \text{ km}$  downwind. The depth of the GSC increases with distance, as did the reflectivity, as shown in Figure 9. The vertical variation of reflectivity is depicted in Figure 10. Highest values are observed near the ground, the decrease with height becoming most pronounced above about 200 m.



**Figure 5.** Vertical particle velocity during passes #3 (top) and #4 (bottom) corresponding to the reflectivity images shown in Figure 3. Positive velocity is upward, negative downward. The turbulent boundary layer is well demarcated in pass #3 through the sharp change to a smooth field above it. That smooth velocity field also provides an indication that noise in the velocity data was quite low.

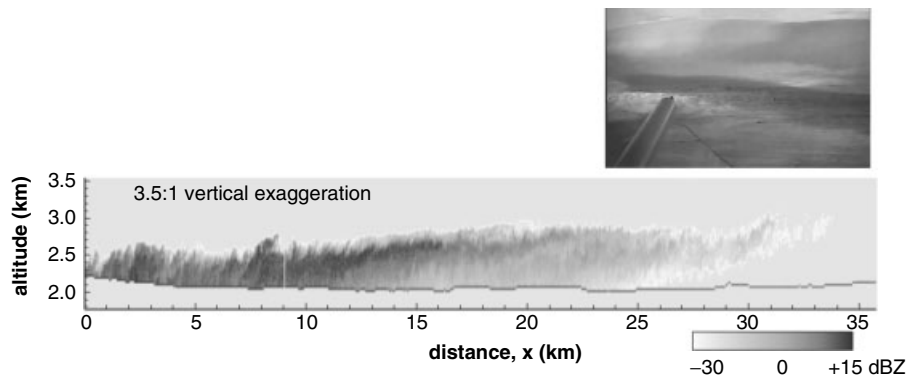


**Figure 6.** Vertical cross-section of reflectivity in a GSC observed on 6 February 2008 at 1726 UTC over relatively flat terrain. The vertical scale is expanded by a ratio of 3.5 compared to the horizontal.

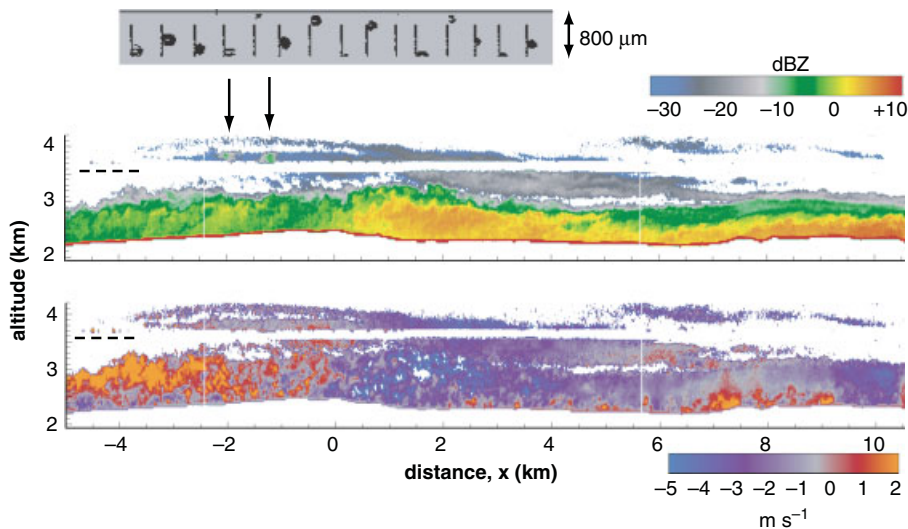


**Figure 7.** Reflectivity and vertical velocity fields from an aircraft pass at 1738 UTC on 6 February 2008 at a location near to that depicted in Figure 6. The horizontal gap in radar data at 3.5 km altitude is the radar dead-zone about the aircraft flight level. At the locations marked with arrows there is evidence for ice crystals lifted into the thin layer of cloud above flight level. See text for further details.

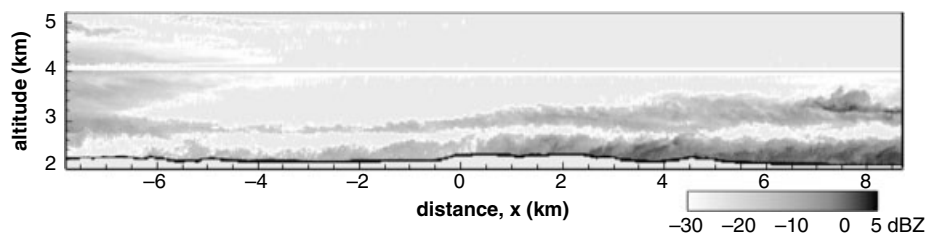


**Figure 8.** Region of formation of a GSC observed on 6 February 2008 at 1753 UTC at a location near the sections shown in Figures 6 and 7 but along a slightly different flight direction. Flight altitude was at 4.1 km.

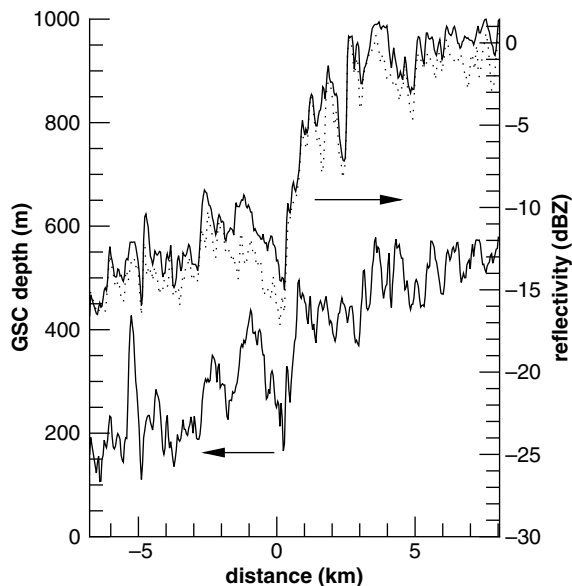


**Figure 9.** The depth of the GSC (left-hand scale) and of the reflectivity within it (right-hand scale) as a function of distance along the wind for the data shown in Figure 8. The full line for reflectivity is the maximum at any given point, while the dotted line is the value at 120 m above the surface.

### 3.3. Sierra Nevada: 9 March 2006

The following two examples are from the Terrain-Induced Rotor Experiment (Grubišić *et al.*, 2008) over the Sierra Nevada. To meet project objectives, the flights were made on days with strong winds. The first example to be shown here consists of a westbound leg, followed immediately by an eastbound one. The total lapse of time for the two legs was 9 min. Flight altitude was near 5 km where the temperature was  $-20^{\circ}\text{C}$  and winds were from  $290^{\circ}$  at  $30\text{ m s}^{-1}$ .

Radar returns were almost identical for the two passes; Figure 11 shows the reflectivity data for the eastbound pass. A roughly 100 m thick layer of smooth echo is present almost everywhere right over the surface with reflectivity near  $-20\text{ dBZ}$ . In addition, deeper plumes are present over the downwind slopes starting at  $x = 7$  and  $x = 12\text{ km}$ .

Video frames, one looking upwind (toward the west, left side of the figure) the other downwind (toward the east) from roughly the same spot, near  $x = 7\text{ km}$ , from the flight altitude of 5 km, show the altocumulus present below the flight level. No radar echo was detected from these clouds for  $x < 7\text{ km}$ . On the other hand, the video frame looking east

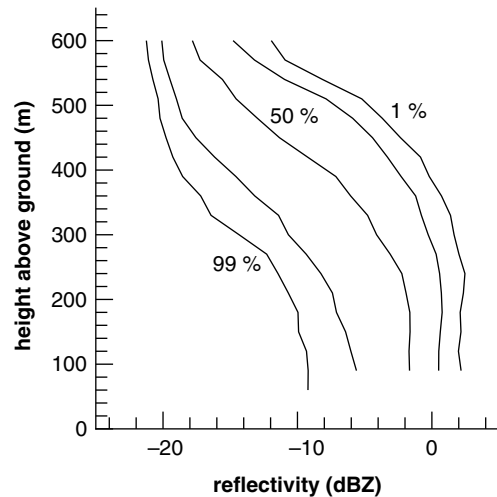


**Figure 10.** The vertical profile of reflectivity for the data shown in Figure 8. The 1, 25, 50, 75 and 99-percentile values are shown for the segment between  $x = 0$  and  $x = 8\text{ km}$ .

shows that there were no clouds right along the flight line in that region, yet echoes to about  $x = 4.2\text{ km}$  were detected. The small mountain peak seen in this frame is located at  $x = 11.5\text{ km}$  in the echo cross-section. Snow blown off the mountain can be seen in the photo and is seen as a strong echo right above the surface at  $x = 12\text{ km}$ .

### 3.4. GSC in high winds over the Sierra Nevada: 15 March 2006

The second example from the Sierra Nevada is shown in Figure 12 from a pair of flight legs into the westerly winds at 6 km altitude and back at 7 km. Winds at these altitudes were roughly from  $260^{\circ}$  at  $35\text{ m s}^{-1}$ . An upwind sounding (LeMoore, CA, USA) shows an inversion between 4 and 5 km altitude at  $-18^{\circ}\text{C}$ . Temperature at 3 km was  $-10^{\circ}\text{C}$ . That sounding indicates a lifting condensation level of near 2 km altitude.

The two flight legs took 22 min. They yielded very similar radar images; data from the second leg is shown in Figure 12. Because of the large distance from flight altitude to the ground, range-gate spacing was set to 45 m; hence the images are of somewhat lower resolution than other cases shown in this paper. The top panel shows the entire cross-section with 3.5:1 vertical stretch; the lower panels show selected segments with 1:1 axis ratio. The radar

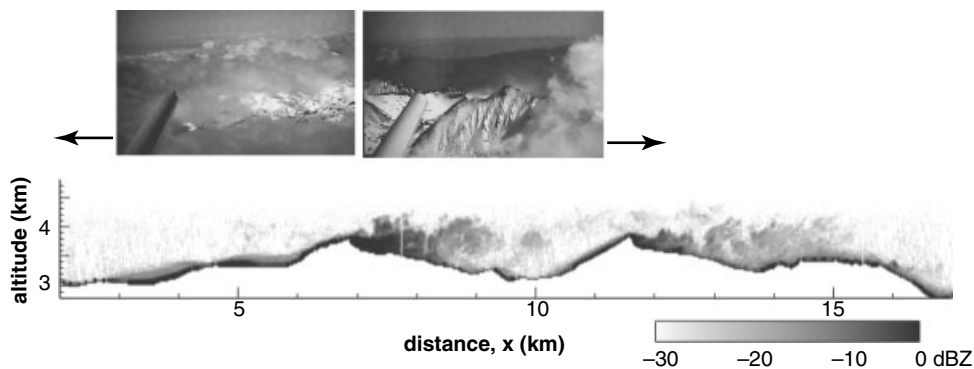


**Figure 11.** Radar echoes from blowing snow and possibly from the altocumulus into which it is lifted. Snow plumes rise principally on the downwind slopes. Data are from the Sierra Nevada, observed on 9 March 2006. Photos taken from the King Air flying at 5 km altitude illustrate the view toward the west and toward the east, both from roughly  $x = 7\text{ km}$ .

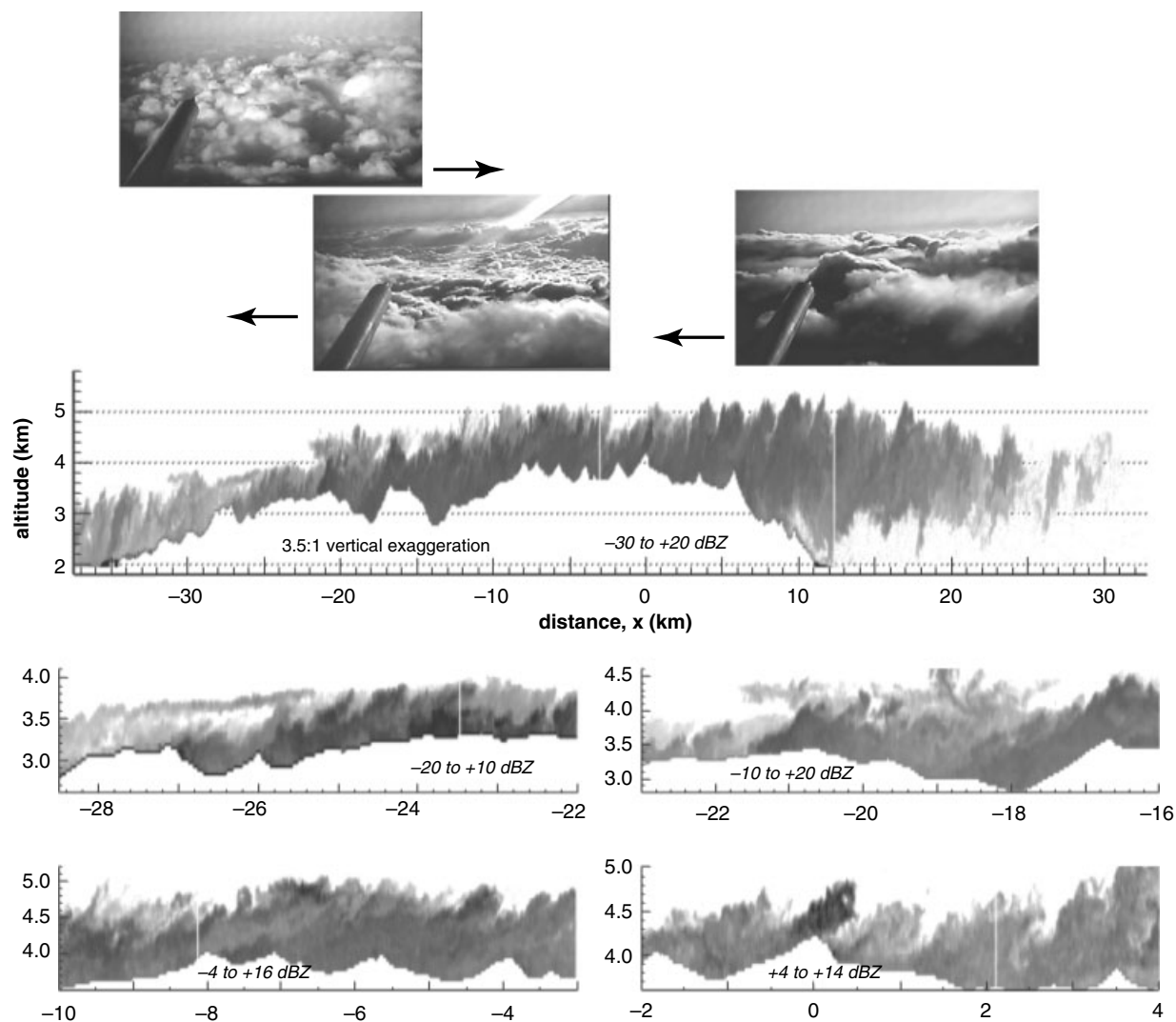


**Figure 12.** GSC observed on 15 March 2006 (0120–0140 UTC) over the Sierra Nevada. The long horizontal panel shows all of the region observed with a 3.5:1 vertical exaggeration. Smaller panels focus on selected regions and are plotted with 1:1 scale ratio. The range of the reflectivity greyscale varies from panel to panel, as indicated. Photos were taken from the flight altitude of 6.05 km at locations ( $x$ -values) roughly at the beginnings of the arrows.

echo extended to heights  $\sim 1$  km above the surface of the mountain throughout the first 40 km of the region depicted. The echo has virga-like character over the downwind slope past  $x = 5$  km. Within the general increase in reflectivity until about  $x = 0$  km there are local maxima corresponding to sudden terrain features.

Video frames included in Figure 12 show the presence of altocumulus below the flight altitude. In the two frames looking west, into the setting sun, the cloud layer looks almost unbroken and is a mix of sharper and more diffuse cloud elements, the former presumably consisting mainly of cloud droplets and the latter dominated by ice crystals. The two frames looking west were taken from 6 km, the upper frame looking east from 7 km altitude. From the higher perspective and with illumination from behind, the cloud layer looks less contiguous and the diffuse cloud elements less abundant. Since the radar echoes were essentially identical for the two passes, the different appearance of the cloud layer can be attributed to changed illumination and point of view.

Vertical Doppler velocities show the turbulent pattern seen in other cases but with important differences, not least of which is that the velocities observed are significantly

greater. The colour scale in Figure 13 spans  $-8$  to  $+8$   $\text{m s}^{-1}$  but some downward velocities exceeded the unambiguous limit of  $-12.15$   $\text{m s}^{-1}$ ; this can be noticed in Figure 13 as the red spots within blue areas that show up between  $x = -4$  and  $x = 15$  km at various altitudes. It can also be noted from Figure 13 that downslope regions have enhanced turbulence. Clearest examples of this are at  $x = -20$  and  $0$  km.

### 3.5. Medicine Bow Mountain sequence: 2 February 2006

Data from this day have special interest in that the nine cross-sections were obtained within a 3 h period. The overall evolution of clouds, as can be seen in Figure 14, is characterized by a decrease in echo extent. The upper-level cloud essentially disappears so that the large echo produced by the merger of the upper level cloud with the lower one changes to a shallow layer close the mountain surface.

The formation of the GSC can be most readily identified in pass #4. The portion of interest for this pass and for those preceding and following it are shown at 1:1 scale in Figure 15. Pass #4, shown in the middle strip, is very similar to pass #4 of the 18 January 2006 case shown in Figure 3. A small detached

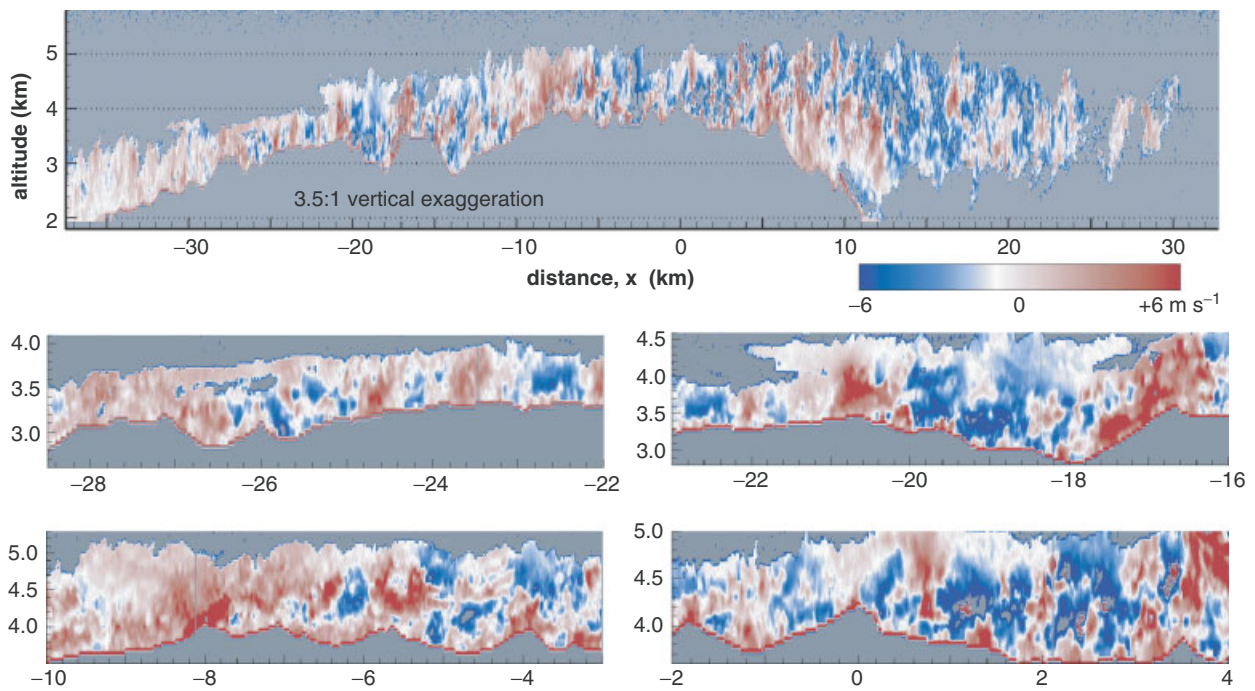


**Figure 13.** Vertical velocity displayed in the same arrangement as that of Figure 12. The velocity scale is from  $-6$  to  $+6 \text{ m s}^{-1}$ . In the bottom right panel some evidence of velocity folding can be seen (red patches within blue regions), indicating downward velocities in excess of  $-8 \text{ m s}^{-1}$ .

echo rises from the surface at  $x = -28.5 \text{ km}$ , several other patches are found right at the surface near  $x = -25 \text{ km}$ , and a contiguous GSC is established by  $x = -23 \text{ km}$ . This pass was made at  $5.1 \text{ km}$  altitude, while all others were at  $4.3 \text{ km}$ ; thus no *in situ* data are available from the aircraft. The only photograph relevant to pass #4 is the video frame taken while the aircraft was lining up for the pass from the west. This photo is included above the image of the echo in Figure 15. Importantly, it shows that the lower cloud deck extended back to at least  $x = -43 \text{ km}$ . The automated weather station at the airport in the upwind valley (roughly  $x = -50 \text{ km}$ ) reported scattered cloud ceiling at  $2.5 \text{ km}$  altitude, with broken cloud at  $3.6 \text{ km}$  and overcast at  $4.0 \text{ km}$ . Temperature at the airport ( $2.1 \text{ km}$  altitude) was  $-1^\circ\text{C}$ , so the cloud base of the lowest layer can be inferred to have been near  $-5^\circ\text{C}$ . The aircraft sounding taken in the valley leads to the same estimate. Winds were from  $290^\circ$  to  $300^\circ$ , with speeds that varied from  $8$  to  $12 \text{ m s}^{-1}$  at different altitudes (up to  $5 \text{ km}$ ) and different times. The radar cross-sections essentially coincide with the air flow.

According to weather reports from the Saratoga airport and from photos taken from the aircraft at the time of pass #3 (about 40 min earlier than #4) the base of the lowest cloud layer was about  $100 \text{ m}$  higher than in #4. Also, higher clouds were more extensive. In the radar image for pass #3 it is difficult to identify any pattern similar to those in #4. The strongest echoes are found near the top of the turbulent layer and echo streaks reach the ground. As shown in Figure 16, LWC up to  $0.4 \text{ g m}^{-3}$  and ice particle concentrations up to  $25 \text{ L}^{-1}$  were detected at flight level ( $4.3 \text{ km}$ ,  $-20^\circ\text{C}$ ). The ice consisted of small graupel up to  $\sim 500 \mu\text{m}$  in diameter.

Pass #5 for which the radar echo is depicted in the lowest panels of Figure 15 was also spaced from #4 by 40 min. By this time the echo extent is reduced compared to earlier passes. A layer of echoes near  $4 \text{ km}$  altitude forms from initially small patches, with the reflectivity gradually increasing and with a structure that is consistent with rising plumes or

rolls. At the  $4.3 \text{ km}$  flight level, pulses of LWC exceeding  $0.5 \text{ g m}^{-3}$  were detected in the turrets, as shown in Figure 16. The concentration of ice particles increased from  $\sim 5 \text{ L}^{-1}$  at  $x = -22 \text{ km}$  to  $\sim 20 \text{ L}^{-1}$  at  $x = -15 \text{ km}$ . The particle shadow images from the 2D-C probe (Figure 16) indicate lump graupel of maximum  $200 \mu\text{m}$  size in the first pulse and up to  $1 \text{ mm}$  in size further downwind. In each turret some LWC was detected together with the ice particles. The vertical velocity trace supports the interpretation of the intercepted cloud segments as convective turrets. The photo included at the bottom of Figure 15 shows that low-level clouds were present at least as far west as  $x = -30 \text{ km}$ . To reach a detectable echo of  $-25 \text{ dBZ}$ , near  $x = -25 \text{ km}$ , the clouds were transported about  $5 \text{ km}$ , roughly  $8 \text{ min}$ , from the point of formation. Subsequent passes showed the same.

A comparison of data from the three passes discussed in the foregoing is shown in Figure 16. The top panel shows the maximum value of the reflectivity between  $45 \text{ m}$  above the ground and flight level,  $z_{\text{max}_{g-fl}}$ , at various points along the transect. The other panels contain *in situ* data along the flight line for passes #3 and #5; in pass #4 the flight level was well above the GSC in a different cloud layer, so that the *in situ* data have no relevance for this discussion. The data in Figure 16 and the images in Figure 15 provide a good basis for examining the impact of lofted snow and also to show the limitation of the available data. In pass #3,  $z_{\text{max}_{g-fl}}$  is already quite high at the beginning of the data segment but increases steadily even beyond that. In the other two passes  $z_{\text{max}_{g-fl}}$  starts with low values, increasing rapidly at first and more gradually later. The presence of detectable plumes near the surface in pass #4 is clear. The first of these is about  $5 \text{ km}$  further upwind and  $1.9 \text{ km}$  below the first point where the cloud rose to flight level in pass #3, and  $10 \text{ km}$  or more further upwind from where the cloud was penetrated on pass #5. In both passes #3 and in #5 ice concentrations increase with distance along the wind. These patterns of  $z_{\text{max}_{g-fl}}$  and of ice concentrations are consistent with the possibility that

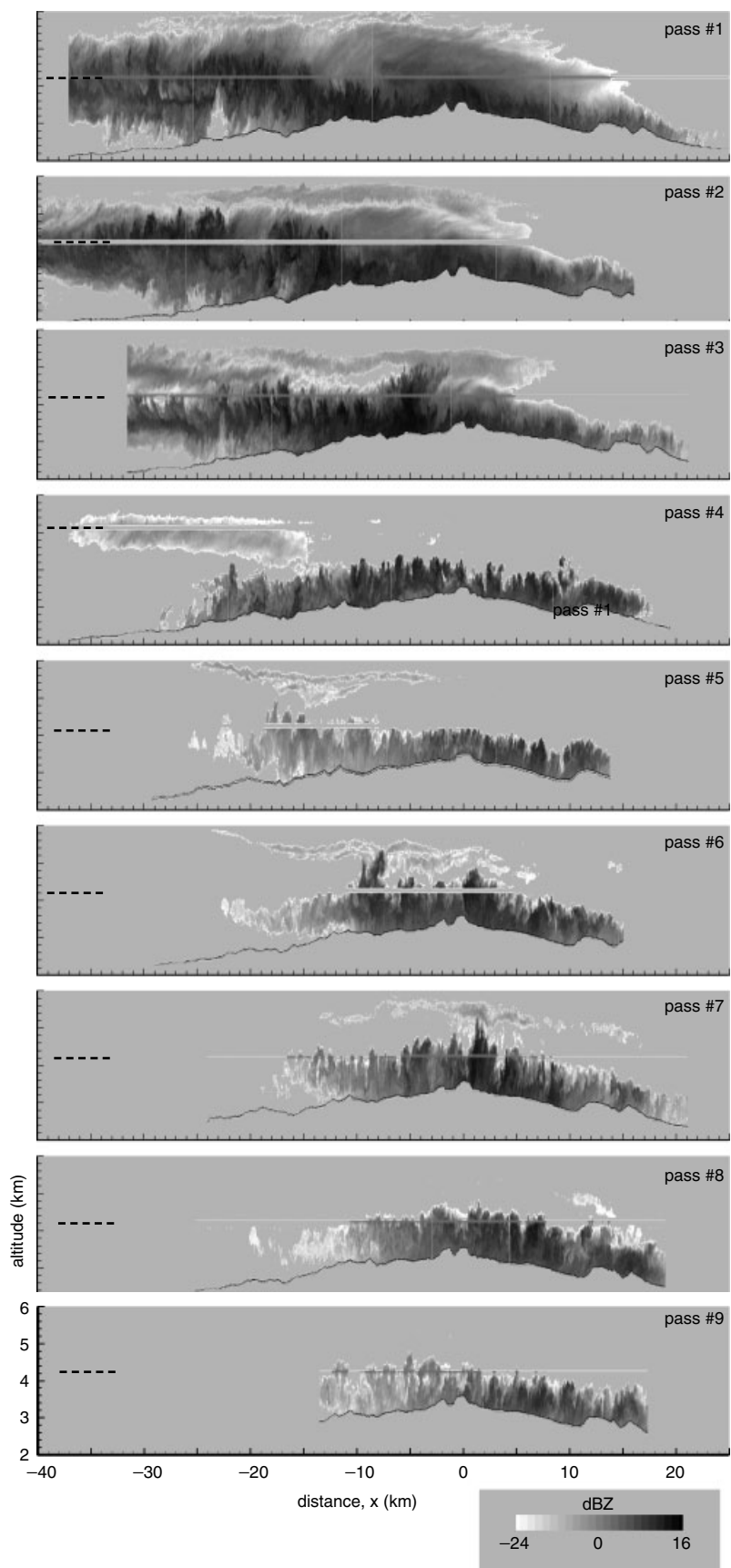
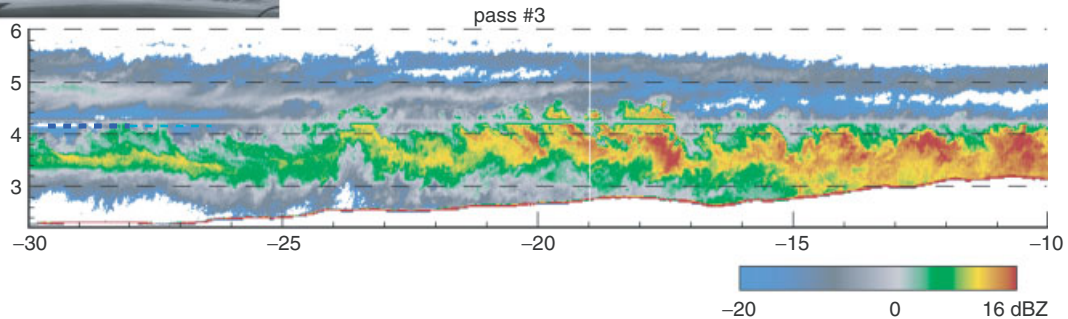
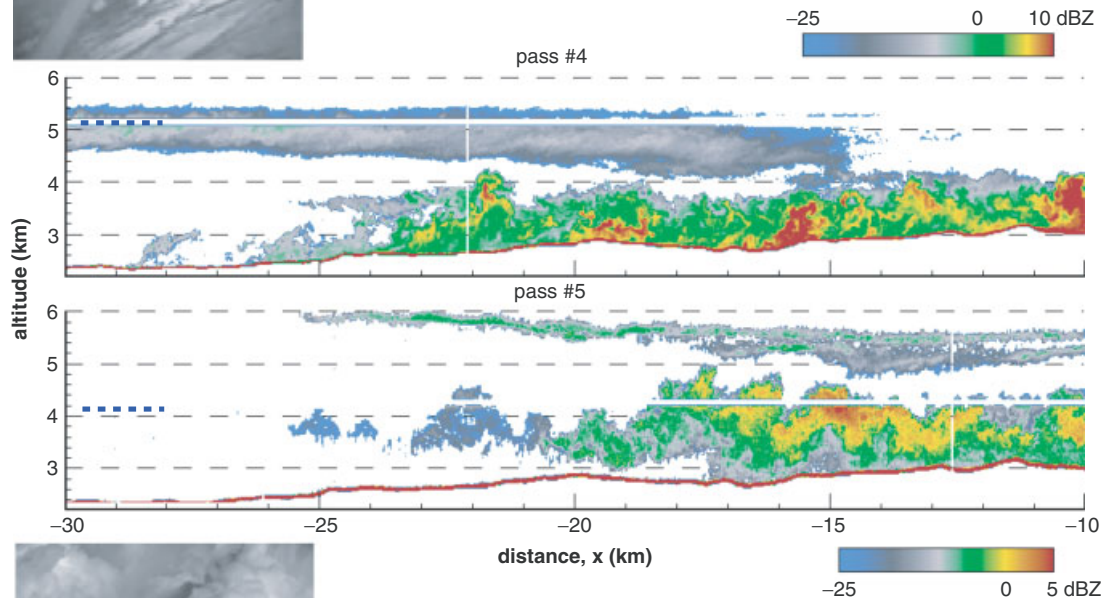


**Figure 14.** Sequence of reflectivity cross-sections from 2 February 2006 over the Medicine Bow Mountains. The images have 3.5:1 vertical exaggeration and the reflectivity grayscale is from  $-24$  to  $+18$  dBZ for all. Times (UTC, rounded to the nearest minute) for  $x = 0$  in each pass are 1905, 1921, 1931, 2013, 2054, 2108, 2118, 2130 and 2141. The longer time gaps between passes #3 and #4 and again between #4 and #5 are due to soundings made by the aircraft in the intervening period. Flight altitude is indicated by the dashed line segment next to the ordinate.

19:38:38 from 3.7 km alt. at x = -41 km



20:07:15 from 5.1 km alt. at x = -43 km



21:01:14 from 4.25 km alt. at x = -37.5 km



**Figure 15.** Details from Figure 14 showing three different stages of the GSC. Note the decreased maxima of the reflectivity scale from top to bottom panel.

the ice observed at flight level originated at the surface. This is also possible for pass #3, but the layer of high reflectivity near 3.5 km altitude right at the beginning of the segment indicates that there was some ice transported into the sample area from further upwind. Because of the evidence for clouds to form considerably upwind of the where echoes are first detected in pass #5, the alternative explanation not involving lofted snow requires some nucleation sequence with a long time for activation.

To provide some insight into the build-up in the amount and growth of snow lofted from the surface, Figure 17 shows the values of reflectivity 90 m above the surface against distance and ground height during passes #3 (also representative of the two earlier passes), #4 and #5 (representative of later passes as well). The rate of increase of reflectivity is  $\sim 1 \text{ dBZ km}^{-1}$  for all three passes. Given reflectivity values were reached in pass #4 about 7 km further upwind than in pass #3, but then there is a shift of  $> 15 \text{ km}$

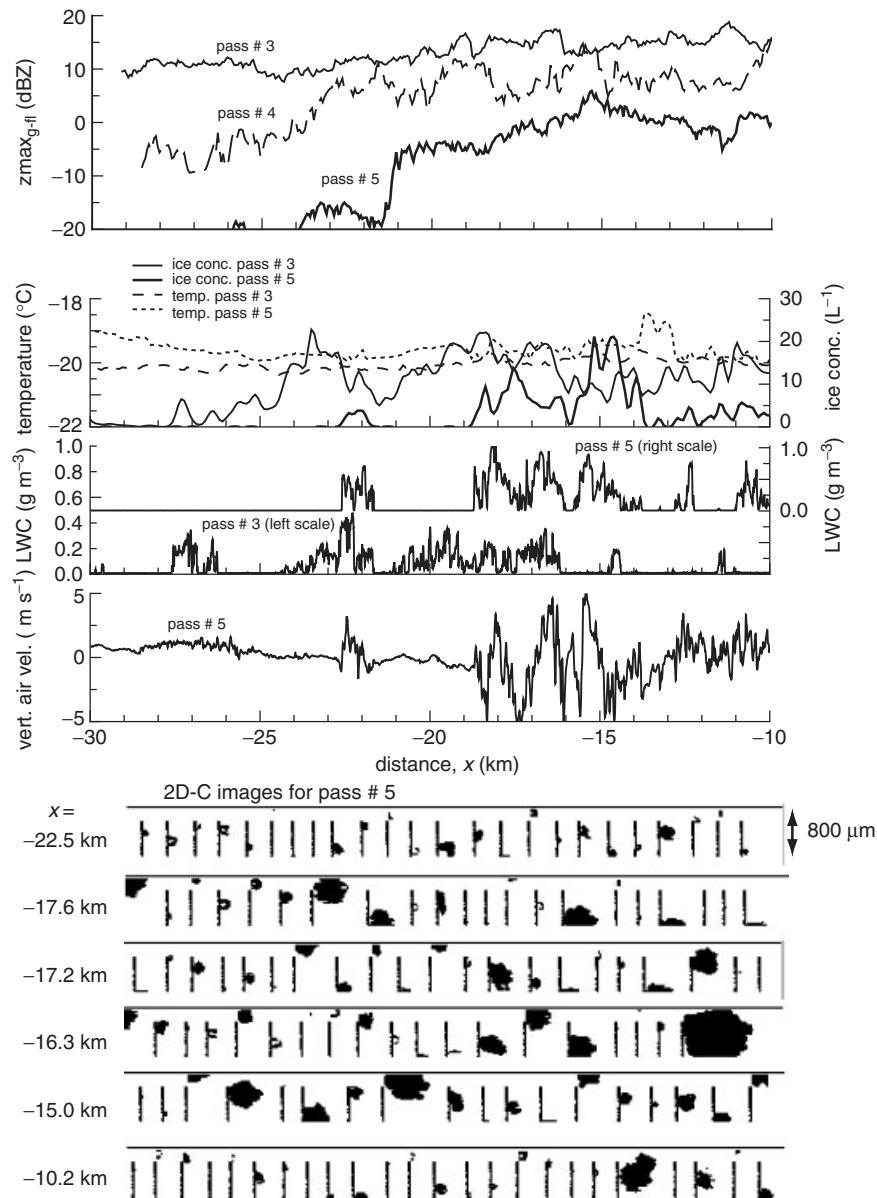


**Figure 16.** Time series of radar reflectivity (top panel) and of *in situ* data for the three flight segments shown in Figure 14. The radar reflectivity value displayed is  $zmax_{g-ll}$ , the maximum observed between 45 m above the ground and the flight level. *In situ* data are from 4.3 km altitude for passes #3 and #5; no data are shown for pass #4 because the 5.1 km flight level of that pass was well above the GSC. Particle images from the 2D-C probe are shown for pass #5, which had the longest flight path within the GSC.

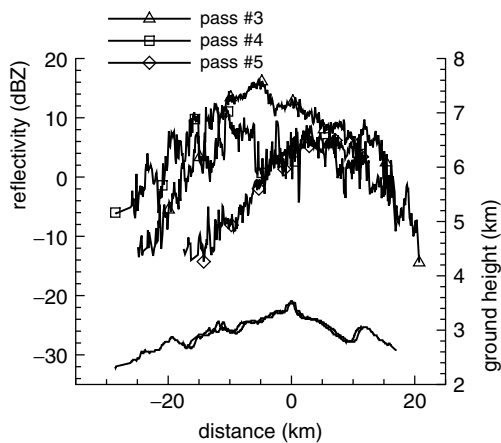


**Figure 17.** The variation of reflectivity at 90 m above the ground during the three passes depicted in Figure 15. The rate of increase is close to  $1 \text{ dBZ km}^{-1}$  in all three cases over the first 20 km after initial detection.

downwind for pass #5. This underscores the uniqueness of the observations during pass #4.

In contrast to the variations observed in the upwind portions of the clouds, the downwind part of the GSC remained essentially the same throughout the period. As seen in Figure 17, at about 5 km east of the peak the reflectivity 90 m above the surface was roughly 7 dBZ in all passes. Reflectivity decreased to near  $-20 \text{ dBZ}$  in an additional 15 km.

### 3.6. Isolated GSC, Medicine Bow: 27 January 2006

A cooling trend of about  $8^\circ\text{C}$  over 10 h produced extensive cloudiness over both the Sierra Madre and Medicine Bow ranges on this day. During an interval of reduced cloudiness a GSC isolated from other clouds was observed and provides a good illustration of the relationship between a supercooled

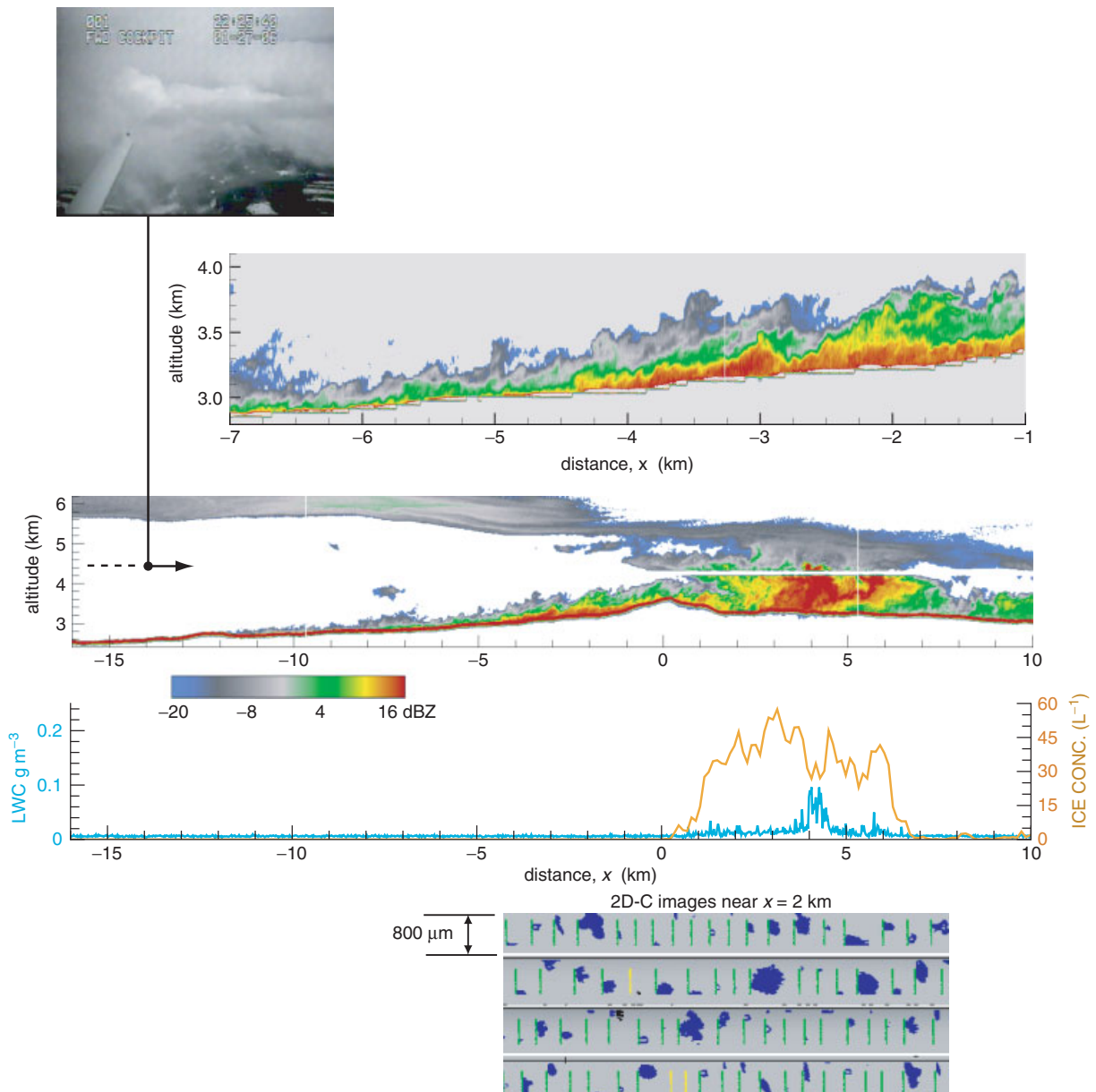


**Figure 18.** Video frame, radar echoes and *in situ* data for the flight segment of 27 January 2006 2222–2231 UTC. Flight altitude was 4.3 km, indicated by the dashed horizontal line next to the ordinate. The radar image in the upper panel is an enlarged segment for the 6 km segment of the data.

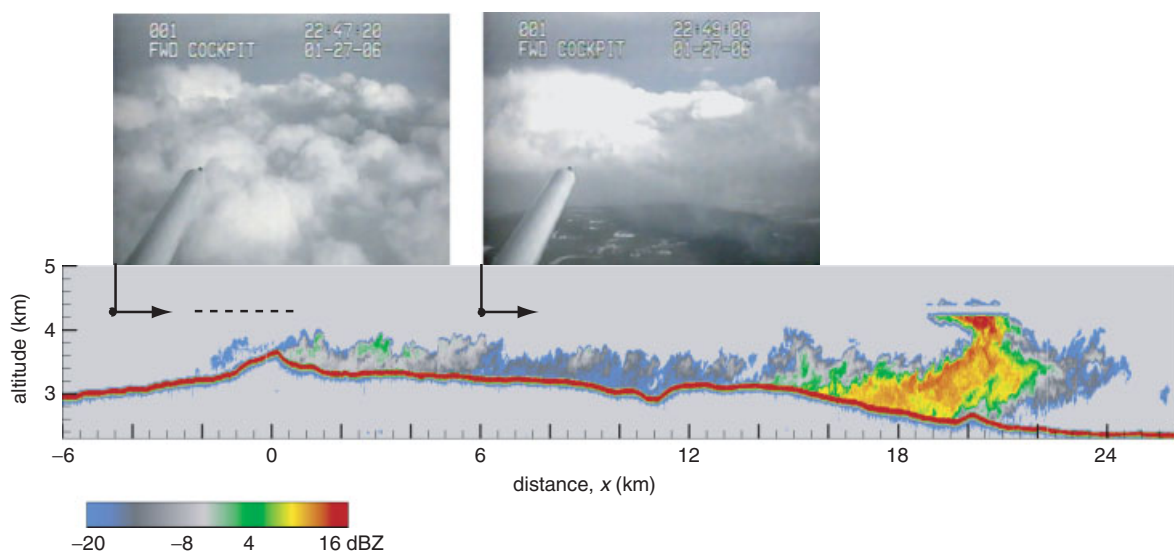


**Figure 19.** Video frames and radar reflectivity for 27 January 2006 2244–2252 over the same region as shown in Figure 18.

cloud layer and the GSC, and of possible glaciation of a cell by ice from the GSC.

During the flight leg depicted in Figure 18 broken stratocumulus clouds were seen with tops below the flight level of 4.3 km. The ground was visible between clouds. The video frame in Figure 18 was taken from  $x = -13.9$  km. No cloud droplets and no ice particles were detected with the *in situ* probes until just past  $x = 0$ , as shown in the middle panel of Figure 18. The radar image shows the GSC beginning at  $x = -12$  km and increasing both in depth and in reflectivity until it merges into a deep cell near  $x = 1.5$  km. The magnified view in the top echo image of Figure 18 shows the internal structure of the GSC. Highest reflectivities are found near the ground and numerous overlapping plumes are clearly evident. Temperature at flight level was  $-17.5^{\circ}\text{C}$  on the western end and  $-16.5^{\circ}\text{C}$  at the eastern end of this flight segment; temperature at the leading edge of the GSC is estimated as near  $-7^{\circ}\text{C}$ . In the large echo between  $x = 0$  and  $x = 7$  km, ice particle concentrations of  $30\text{--}50\text{ L}^{-1}$  were detected along with a small patch of supercooled cloud.

The same flight path was followed again 20 min later; data from this leg are shown in Figure 19. The visual appearance of the clouds below flight level changed little and these clouds extended on the west side to at least  $x = -12$  km. However, the radar echo from the GSC starts only near  $x = 0$  km, having moved eastward by about 10 km, and covers the downwind slope of the mountain. Reflectivity in the GSC is not increasing steadily from west to east but has a region of low values between  $x = 6$  and  $x = 13$  km. In this region the ground is clearly visible, i.e. the GSC is sub-visible. During the cloud penetration at  $x = 19$  km, ice particle concentrations peaked at  $30\text{ L}^{-1}$ .

In both passes, the GSC merges into a deep echo, just past the mountain peak in Figure 18 and at  $x = 20$  km in Figure 19. A flight leg between the two shown here had the same pattern, with the deep cell at  $x = 12$  km. The translation of the cells corresponds to about  $12\text{ m s}^{-1}$ ; wind speed at the flight level was  $18\text{ m s}^{-1}$ . Rather than the same cell being intercepted on the three passes (flight legs were at about  $20^{\circ}$  off the wind direction) it appears in satellite images that the cells were elements of a line of convection. It is intriguing to speculate about the contribution by the GSC to the development of ice and precipitation in the cells. The GSC becomes the lower part of the deep cell (as seen in the echo structure) and it is likely that ice particles are lifted into the cells. However, the cells rose to near  $-20^{\circ}\text{C}$ , and even colder in Figure 18, so some ice development can be expected near the cloud top as well.

#### 4. Origins of GSCs

From observations described in the preceding section and from other cases that have been analysed, the main characteristics of GSCs can be summarized as follows:

- Temperatures at the surface in the regions where GSCs are detected are in the range  $-3$  to  $-10^{\circ}\text{C}$ , and the ground is covered by snow. Wind speeds near the surface are estimated to be  $>10\text{ m s}^{-1}$ .
- Radar reflectivities observed in the GSCs are well above values that could originate from water clouds. The reflectivity that could be expected for 1 km adiabatic lift,  $0^{\circ}\text{C}$  cloud base and  $500\text{ cm}^{-3}$  droplet concentration is roughly  $-35\text{ dBZ}$ . Thus it is certain

that the reflectivity patterns observed in the GSCs are due to ice particles.

- Supercooled liquid and mixed-phase clouds were at times seen upwind at the level of the GSCs and at flight levels along substantial portions of the GSCs. On the rising slopes of mountains, the altitude of formation of the GSC approximately coincides with estimated cloud base height. However, the complexities of airflow over mountains, coupled with rapid changes in the upper troposphere during winter storms, make cloud base estimates prone to error. Even so, available data support the assumption that the regions of formation of GSCs are supersaturated with respect to ice, so that ice particles will grow within the GSC. At the point of first formation of the GSCs, the presence of cloud droplets is uncertain, and even if present the liquid water content can be expected to be minimal.
- Reflectivity values within the GSC range from roughly  $-25\text{ dBZ}$ , the minimum signal that can be reliably detected, to near  $+20\text{ dBZ}$ , which is near the maximum observed in ice clouds of any type. Reflectivity  $\sim 100\text{ m}$  above the surface increases with along-wind distance roughly  $1\text{ dBZ km}^{-1}$  over the upwind slopes.
- Sharp terrain features (peaks or ridges) frequently have high reflectivity patches just upwind or downwind from them.
- For wind speed increasing with height above the surface, as confirmed by dual-Doppler analyses, the observed curvature of high-reflectivity regions in the formation region off GSCs is consistent with rising plumes.
- Variations of Doppler vertical velocity within the GSCs indicate significant levels of turbulence. The influence of terrain is clearly seen in many cases.
- On the downwind side of the mountain, the turbulent echo-filled layer extends to altitudes lower than that of the formation of the GSC and it is present even in cases when the GSC is not clearly evident on the upwind side.
- The GSC are often visually undetectable yet produce appreciable radar echoes.

Based on the aforesaid, GSCs can be defined as ice clouds within a turbulent boundary layer exhibiting some or all of three signatures: (i) the existence of an isolated GSC in the upwind region, not connected to radar echoes above it and with visible or *in situ* evidence for clear air just above the GSC; (ii) higher reflectivity in the GSC than in the region above it when the echoes are merged; and (iii) plume-like features rising from the surface. These three signatures distinguish the GSC from a boundary layer into which snow is falling from above. The first two criteria are not totally fail-safe, as it is possible for undetected ice crystals to fall into a supercooled liquid cloud and quickly grow there; hence that possibility needs to be considered on a case-by-case basis. The third criterion is quite stringent. For falling particles to produce trails with the observed curvature in a wind field of increasing velocity with height above the surface, the particles would have to undergo rapid growth and increasing fall velocity as they approach the surface – a scenario that is hard to reconcile with realistic conditions of cloud liquid water content and growth by riming, so that it can be practically ruled out. The consistent shapes, spacing and

dimensions of these plumes provide evidence that they are not happenstance events within the turbulence. The possible role of crystal aggregation within the GSC is difficult to assess because it does not produce a clear signature either in fall velocity or in W-band reflectivity. Fall velocities do not increase significantly with aggregation and remain relatively small compared to the turbulent velocities observed in GSC. Reflectivity at W-band, being influenced by density and by Mie effects, does not increase with aggregation according to observations (Wolde and Vali, 2002). No images of aggregates have been found in the flight-level *in situ* data, but more definitive assessments of aggregation will have to await surface observations from within GSC.

In the following, the potential initiation mechanisms – the same ones given in RV87 – are examined in light of the data presented in this paper.

#### 4.1. Blowing snow

Blowing snow can be expected to be a component of the explanations for the observations here reported, since it is commonly found to be present in similar situations. However, existing knowledge about blowing snow is insufficient for describing the GSC. Literature on blowing snow (also called ‘drift’) refers almost exclusively to observations in clear air, so that the lofted particles are undergoing sublimation. In contrast, the GSC form in the presence of supercooled clouds or in air supersaturated with respect to ice. Thus existing data are not directly applicable, but the difference is in fact helpful for constructing a potential explanation of the GSC, as will be argued after reviewing some of the literature on blowing snow.

Yang and Yau (2008) summarize the essential features of blowing snow as follows: ‘When the wind speed exceeds a threshold value, snow particles start to bounce in a series of leaps at the surface and the saltation<sup>†</sup> layer is formed. With stronger winds, turbulent eddies can diffuse the saltated particles upwards and they can become suspended in the atmosphere as the result of the balance of turbulent diffusion and sedimentation. Sublimation of blowing snow particles then results.’

The threshold wind speed for blowing snow of 10 km visibility, measured at 2 m height, is 7–10 m s<sup>-1</sup>, with a weak trend toward lower speeds at colder air temperatures (Déry and Yau, 1999). Other papers report measurable concentrations of lofted snow particles for wind speeds as low as 4 m s<sup>-1</sup> (e.g. Mahesh *et al.*, 2003). Studies of blowing snow particles are generally conducted over flat terrain. The role of topography, with surface features on many different scales, is included in some models of snow mass distribution (e.g. Winstral *et al.*, 2002; MacDonald *et al.*, 2009).

A good set of observations characterizing particle sizes in blowing snow is available from Schmidt (1982). Size distributions were recorded at various heights on an 8 m tower on the lee side of the Medicine Bow Mountains with an optical counter capable of detecting particles 60 µm and larger. Particle concentrations were found to decrease with height to the power  $-0.5$  to  $-1.1$  and mean particle size to fall off with powers of  $-0.2$  to  $-0.28$ . Using averages of these rates of decrease radar reflectivity (calculated as the

sixth moment of size, with no consideration of shape and Mie effects) decreases with height to the power of  $-2.5$ . At a height of 1 m, the measured size distributions lead to roughly 0 dBZ and to  $-23$  dBZ at 10 m. Extrapolating to 100 m above the surface, the reflectivity would be expected to decrease to  $-50$  dBZ. Yang and Yau (2008) show a similar power law dependence on height below 1 m (their Figure 8). More recent measurements of Nishimura and Nemoto (2005) from Antarctica, also using an optical particle counter with minimum detectable size of 50 µm, indicate a similar height dependence below 1 m, but a weaker one between 1 and 10 m.

The papers cited in the foregoing exemplify the focus in studies of blowing snow on heights of only a few tens of metres above the surface. This is justified by the rapid decrease of drift snow flux and of visibility impact with height. A lidar system operated at the South Pole yielded data showing continuous scattering layers indicative of blowing snow up to 600 m above the surface in 10 out of 40 observations (Mahesh *et al.*, 2003), but the authors consider it possible that those cases may have also included clear-sky precipitation (diamond dust) events. Palm *et al.* (2011) obtained measurements of the depth of blowing snow layers over Antarctica with the space-borne CALIOP lidar and report that 25% of the cases had depths of between 100 and 300 m, 4% exceeded 300 m and only 0.8% extended to over 500 m. All these observations were made in cloud-free conditions.

The lofting of snow is dependent on winds at the surface and on the condition of the snow. The latter is determined by many factors; most importantly by the type of snow that fell, the temperature and humidity history from the time of deposit, the depth of the snow deposit and underlying soil temperature, solar radiation and tree shadows. No data are available on these for cases here discussed. Winds right at the surface are also unknown but dual-Doppler analyses of the radar data provide some insight into wind conditions. This is illustrated by the data shown in Figure 20 for the case in

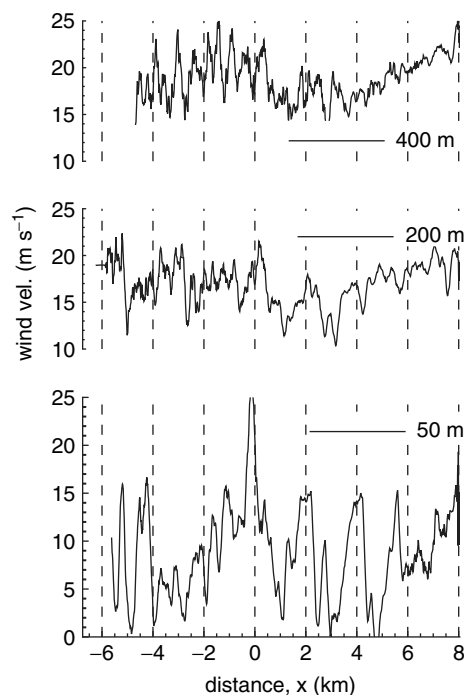


**Figure 20.** Horizontal wind velocity at various heights above the ground determined by dual-Doppler analysis for 6 February 2008 covering the same data segment as that shown in Figure 8.

<sup>†</sup>Saltation is the leaping movement of particles as they are transported by the wind over the surface.

Figure 8. This case is chosen because airflow over the nearly flat terrain is simpler than over mountains. The points these data illustrate are that wind velocity increases with height above the ground, that variability is greater lower down, and that variability is present on many scales, some clearly due to wave activity influencing the entire boundary layer. It is also seen that wind velocity in this case, and others we looked at, exceeds  $10 \text{ m s}^{-1}$  at the lowest altitude level of data, at least in local maxima. Especially noteworthy in Figure 20 is the presence of local peaks in velocity at 50 m above the surface, as such bursts are a possible source for plumes of greater reflectivity like those that can be seen in Figure 8, although the plumes are associated with bursts that existed some time earlier. A comparison of the velocity traces at the three levels suggests a decrease in the dominant scale of turbulence with height above the surface.

In all, current literature on blowing snow studies provides information on the basic elements of the process but it gives only scant direct support to the idea that it plays an important role in the formation of GSC. That is mainly due to the limited vertical depth that these studies cover and the large particle sizes that were measured. Evidence for snow particles getting lofted can be seen in the plumes of high reflectivity, such as those seen, for example, in Figure 11. Since measurements of particle sizes in blowing snow (see earlier citations) are available only for sizes of several tens of micrometres and larger, it has to be assumed that the observed size distributions can be extrapolated to smaller sizes to the range that is compatible with the RV87. In addition to direct lifting from the snow surface, the break-up of larger crystals during saltation or during collisions may contribute to the population of small sizes which are most readily mixed throughout the depth of the turbulent surface layer. These processes provide a plausible qualitative explanation for the formation of GSCs; however, quantitative representations of the lofting, of the turbulent plumes and of particle growth will be required to test the hypothesis.

#### 4.2. Ice nucleation

One argument for ice nucleation not being a prime contributor to the ice particles observed in the GSC is the frequent presence of supercooled clouds upwind of where the GSC are first detected and that those clouds are at a temperature colder than the GSC. The cases described in sections 3.5 and 3.6 are good examples of this. Another reason to give little weight to the possibility of ice nucleation is that the temperatures at which the GSC are first detected are greater than  $-10^\circ\text{C}$ , where very few active ice nuclei can be expected. Activation of ice nuclei very near the surface, where the snow cover reduces humidity below water saturation, has weak support from laboratory evidence, though evaporation of cloud is considered by some to be conducive for ice nucleation (Cantrell and Heymsfield, 2005; Fridlind *et al.*, 2007).

#### 4.3. Rime splintering

The criteria for Hallett–Mossop type ice splinter production are well known (Hallett and Mossop, 1974; Harris-Hobbs and Cooper, 1987): temperatures between  $-4$  and  $-8^\circ\text{C}$  and droplets of diameters  $>24 \mu\text{m}$ . GSC are observed at those temperatures but also outside that. Cloud droplet

sizes near the condensation level are expected to be smaller, but turbulence may bring droplets of larger sizes to near the surface, where rime can form on trees and rocks. The large extent of the rime surface and many droplet impacts would allow splinter production of even low probability to become appreciable in the GSC. Thus, while current evidence is against this process playing a role, it cannot be totally ruled out. Additionally, it may be speculated that rime splintering would lead to a more uniform echo pattern than the observed plumes and generally non-uniform reflectivity values near the surface.

#### 4.4. Seed crystals from other clouds

The possibility that the ice particles originate upwind or above the initiation region of GSC but grow to radar-detectable sizes in that region deserves to be carefully considered. This is the seeder–feeder process, well recognized in other situations. Merging of the GSC radar echo with echoes from the deeper clouds above it, and occasional fall-streaks of ice from higher clouds reaching the GSC, are seen in some of the examples presented in section 3. There is also radar evidence, not included here, that an outflow of ice particles from clouds over the upwind Sierra Madre range can reach clouds over the Medicine Bow range even when the main cloud masses on the two ranges are separated by several tens of kilometres. Until now, such streams of ice particles across the valley separating the two ranges have been detected only at altitudes of 4–5 km, but it cannot be ruled out that similar streams also occur at lower altitudes. Furthermore, it is possible that streams of ice particles of small sizes and in low concentrations remain undetectable by both aircraft measurements and by radar. Ice crystal precipitation was frequently detected with the *in situ* probes during the upwind aircraft soundings for the Medicine Bow cases we examined. While the potential for transport of these crystals or remnants of them to the GSC cannot be fully rejected, no such occurrence has been detected. Should such seeding from upwind occur, the resulting radar echo in the GSC would likely not have the plume-like structure actually observed.

The most definitive examples of situations where seeding from the top can be excluded are those of the T-REX project described in sections 3.3 and 3.4 and illustrated in Figures 11 and 12. There were either no clouds at all above the surface layer, or at a minimum there were none at flight level and no particles were detected by the *in situ* probes on the aircraft. The same can be said of several of the passes described in section 3.5 and shown in Figure 7. However, in all of these cases the leading edges of GSCs were upwind from the sampled portion and that leaves some uncertainty.

In many cases, there is an echo-free region above the GSC. This is a good indication for the absence of seeding from above, but the degree of assurance it provides is limited by radar sensitivity. The same can be said about the possibility of seeding from upstream, though tens of kilometres free of echo upwind of the GSC make it very unlikely that small crystals not detected by the radar would in fact survive and play a role in initiating a GSC.

### 5. Evolution of GSCs and other characteristics

The temporal evolution of the GSCs provides further insight into the conditions and processes controlling them. As seen

in Table 1, many of the cases were observed over periods two to three times longer than the transit time of the air over the observed domain ( $\sim 1$  h near the surface). Even over these relatively short time periods considerable changes can be seen in most cases.

In the two cases with most detailed time history (section 3.1, Figure 1; section 3.5, Figure 14) the entire cloud system decreased in both horizontal and vertical extent, and the GSC changed from being embedded in the deeper cloud to an isolated form only for brief periods. The isolated GSC requires humidity stratification in which near-water saturation prevails in the near-surface layer and has a drier layer between that and the higher cloud. The brief period of existence for such a stratification (tens of minutes) is not surprising in view of the rate of overall evolution of the cloud system. However, while the isolated GSC is the most striking manifestation of these clouds, the overall duration of the GSCs is longer, of the order of several hours.

As shown in Figures 4, 9 and 16, reflectivity increases at roughly  $1 \text{ dB km}^{-1}$  ( $26\% \text{ km}^{-1}$  in terms of reflectivity). This rate of increase can be ascribed to a combination of increased sizes of transported particles due to continued cooling, coupled with increased concentrations due to the continuous injections from plumes. Over the downwind slopes reflectivity diminishes with distance, as illustrated in Figures 4 and 16. The decrease for these two cases is  $2.0\text{--}2.5 \text{ dB km}^{-1}$ . That rate is twice the rate of increase on the upwind side. The decrease results from the fallout of crystals combined with evaporation.

Maximum reflectivity values do not coincide, as a rule, with the maximum terrain altitude but are located further upwind in early stages and shift to the downwind side later on (see Figures 4 and 16). During those times the GSC extends to lower altitudes on the downwind side than the altitude of first detection on the upwind side.

Vertical velocity and turbulence do not have significant trends with horizontal distance along the mountain slope. Throughout the entire GSC, both parameters fluctuate over the same ranges. The measure of turbulence used to examine this point was the standard deviation of the vertical velocity over sliding box regions of about 100 m dimensions. No correlations were found between reflectivity and vertical velocity except in small regions. This is in part because of the significant levels of turbulence in the GSC and in part because particle fall velocities are not negligible. Dense plumes of snow lifted from the surface do yield local areas of positive correlation but such events are rare; one example can be seen at  $x = -5.7 \text{ km}$  in Figures 4 and 5.

## 6. Conclusions

Data from an airborne, downward-pointing W-band radar were presented that show clouds of ice particles filling turbulent layers of up to 1 km depth above the surface. These clouds are named ground-layer snow clouds (GSC) in order to emphasize that they are in contact with the ground or very near it, that they contain ice particles and that the particles are suspended as in a cloud. The GSC could not have been diagnosed by other observational systems owing to their shallow depth and proximity to the ground. *In situ* observations indicative of such ice clouds have been previously reported by Rogers and Vali (1987; RV87) and by Mahesh *et al.* (2003). The observations originate from

wintertime over mountains with snow-covered terrain. The GSCs are clearly identifiable within, or only slightly separated from, deeper clouds overlying them by their reflectivity structure and by the turbulence within the layer. The GSC may be sub-visible yet radar detectable.

Four processes, also suggested by RV87, were examined as possible sources of the ice particles within the GSCs. It is concluded that lofting and subsequent growth of small snow particles is the most plausible explanation. In contrast to observations of blowing snow under conditions where the ice is evaporating and only large particles are found extending to limited heights over the ground, humidity close to water saturation and the level of turbulence make it plausible that within the GSCs small ice particles produced by direct lifting from the snow surface, or as a result of fragmentation during saltation of snow particles, survive and grow. This difference justifies differentiation of GSCs from what is more commonly considered blowing snow. In other words, with sufficiently high humidity, small lofted snow particles can fill the boundary layer and form the GSC.

In addition to lofted ice particles, entry of pre-existing ice crystals may also be taking place in some fraction of the cases. Nucleation and rime splintering have the least evidence supporting them and both require rather specific conditions to act, so these are considered the least likely processes to be significant.

At this time, no *in situ* data are available that would help ascertain the origin of the ice particles in the GSC; neither can the balance of ice to liquid and the time evolution of that balance be determined. Because liquid water content and cloud droplet sizes near the surface are almost sure to be such that their contribution to the W-band reflectivity is minimal, the observed reflectivity structures are fairly certain to be due to ice particles.

The question of how much influence GSCs have on the clouds and precipitation in the deeper systems that envelop the GSCs is not well illuminated by the data presented in this paper. There is evidence from several cases that ice particles from the GSC reach the clouds above it and, if it is also surmised that the full extent of the GSCs is not seen in the radar images because of limited instrument sensitivity, it is possible that the influence is even more extensive than can be identified in the available data. Turbulence within the GSC and the convection that is sometimes also present are potential facilitators of ice particle injection into clouds above the turbulent layer.

A noteworthy observation in some of the cases is the considerable extent of supercooled clouds upwind of the point where cloud base intersects the mountain slope and the GSC begins to form. The tops of the shallow stratocumuli observed in the case described in section 3.5 reached temperatures near  $-20^\circ\text{C}$ , so the absence, or slow development, of ice in these clouds is an indication for the paucity of ice nuclei.

Future studies of the GSCs are needed in order to more clearly establish the conditions under which they form and to learn how this process of ice crystal generation and cloud glaciation takes place. In addition, the GSCs provide an unparalleled opportunity to study with remote sensing tools (radar and lidar) the turbulent boundary layer containing these clouds, to examine the relationship between turbulence and surface features, and to study the influence of the GSC on the surrounding deeper cloud systems.

## Acknowledgements

The flights in southeast Wyoming were directed by Drs B. Geerts, D. Leon, J. Snider and Z. Wang of the University of Wyoming. Permission to use data from the flights over the Sierra Nevada Mountains was kindly given by Dr V. Grubisic, PI of the T-REX06 project. Dr S. Haimov has made major contributions to the radar operations and data processing. Many thanks to Prof. Kouichi Nishimura of Niigata University, Japan, for providing blowing snow data. Deep appreciation goes to the Wyoming King Air flight crews, Dr A. R. Rodi, and the flight facility supporting personnel for making this work possible. Financial support to the Wyoming King Air Flight Facility is provided by the U.S. National Science Foundation through a Cooperative Agreement. Work on this paper was supported by Grant 0650609 (G. Vali, PI) from the Atmospheric Sciences Division of the U.S. National Science Foundation. The careful review and constructive suggestions of the reviewers have contributed substantially to improving the manuscript.

## References

- Cantrell W, Heymsfield A. 2005. Production of ice in tropospheric clouds: a review. *Bull. Am. Meteorol. Soc.* **86**: 795–807.
- Déry S, Yau MK. 1999. A climatology of adverse winter-type weather events. *J. Geophys. Res.* **104**(D14): 16657–16672.
- Fridlind AM, Ackerman AS, McFarquhar G, Zhang G, Poellot MR, DeMott PJ, Prenni AJ, Heymsfield AJ. 2007. Ice properties of single-layer stratocumulus during the Mixed-Phase Arctic Cloud Experiment: 2. Model results. *J. Geophys. Res.* **112**: D24202, DOI: 10.1029/2007JD008646.
- Geerts B, Miao Q, Yang Y. 2011. Boundary-layer turbulence and orographic precipitation growth in cold clouds: evidence from profiling airborne radar data. *J. Atmos. Sci.* **68**: 2344–2365.
- Grubišić V, Doyle JD, Kuettner J, Dirks R, Cohn SA, Pan LL, Mobbs S, Smith RB, Whiteman CD, Czyzyk S, Vosper S, Weissmann M, Haimov S, De Wekker SFJ, Chow FK. 2008. The terrain-induced rotor experiment. *Bull. Am. Meteorol. Soc.* **89**: 1513–1533.
- Hallett J, Mossop SC. 1974. Production of secondary ice particles during the riming process. *Nature* **249**: 26–28.
- Harris-Hobbs RL, Cooper WA. 1987. Field evidence supporting quantitative predictions of secondary ice production rates. *J. Atmos. Sci.* **44**: 1071–1082.
- Kleissl J, Honrath RE, Henriques DV. 2006. Analysis and application of Sheppard's airflow model to predict mechanical orographic lifting and the occurrence of mountain clouds. *J. Appl. Meteorol. Climatol.* **45**: 1376–1387.
- Lachlan-Cope T, Ladkin R, Turner J, Davison P. 2001. Observations of cloud and precipitation particles on the Avery Plateau, Antarctic Peninsula. *Antarctic Sci.* **13**: 339–348.
- Leon D, Vali G, Lathon M. 2006. Dual-Doppler analysis in a single plane from an airborne platform. *J. Atmos. Oceanic Technol.* **23**: 3–22.
- MacDonald MK, Pomeroy JW, Pietroniro A. 2009. Parameterizing redistribution and sublimation of blowing snow for hydrological models: tests in a mountainous subarctic catchment. *Hydrol. Proc.* **23**: 2570–2583.
- Mahesh A, Eager R, Campbell JR, Spinhirne JD. 2003. Observations of blowing snow at the South Pole. *J. Geophys. Res.* **108**: 4707, DOI: 10.1029/2002JD003327.
- Nishimura K, Nemoto M. 2005. Blowing snow at Mizuho station, Antarctica. *Philos. Trans. R. Soc. A* **363**: 1647–1662.
- Palm SP, Yang Y, Spinhirne JD, Marshak A. 2011. Satellite remote sensing of blowing snow properties over Antarctica. *J. Geophys. Res.* **116**: D16123, DOI: 10.1029/2011JD015828.
- Rogers DC, Vali G. 1987. Ice crystal production by mountain surfaces. *J. Clim. Appl. Meteorol.* **26**: 1152–1168.
- Schmidt RA. 1982. Vertical profiles of wind-speed, snow concentration, and humidity in blowing snow. *Bound.-Lay. Meteorol.* **23**: 223–246.
- Stevens B, Lenschow DH, Vali G, Gerber H, Bandy A, Blomquist B, Brenguier JL, Bretherton CS, Burnet F, Campos T, Chai S, Faloon I, Friesen D, Haimov S, Laursen K, Lilly DK, Loehrer SM, Malinowski SP, Morley B, Petters MD, Rogers DC, Russell L, Savic-Jovac V, Snider JR, Straub D, Szumowski MJ, Takagi H, Thornton DC, Tschudi M, Twohy C, Wetzel M, Van Zanten MC. 2003. Dynamics and chemistry of marine stratocumulus: Dycoms-II. *Bull. Am. Meteorol. Soc.* **84**: 579–593.
- Vali G, Kelly RD, Pazmany A, McIntosh RE. 1995. Airborne radar and in-situ observations of a shallow stratus with drizzle. *Atmos. Res.* **38**: 361–380.
- Vali G, Geerts B, Leon D, Snider JR. 2008. 'Surface sources of ice particles in mountain clouds'. In *15th International Conference on Clouds and Precipitation (ICCP)*, Cancun: Mexico.
- Winstral A, Elder K, Davis RE. 2002. Spatial snow modeling of wind-redistributed snow using terrain-based parameters. *J. Hydrometeorol.* **3**: 524–538.
- Wolde M, Vali G. 2002. Cloud structure and crystal growth in nimbostratus. *Atmos. Res.* **61**: 49–74.
- Wood R, Bretherton CS, Leon D, Clarke AD, Zuidema P, Allen G, Coe H. 2011. An aircraft case study of the spatial transition from closed to open mesoscale cellular convection over the Southeast Pacific. *Atmos. Chem. Phys.* **11**: 2341–2370.
- Yang J, Yau MK. 2008. A new triple-moment blowing snow model. *Bound.-Lay. Meteorol.* **126**: 137–155.